Oil & Natural Gas Technology

DOE Award No.: DE-FC26-05NT42663

Final Report

Seismic-Scale Rock Physics of Methane Hydrate

Submitted by:
Geophysics Department.
Stanford University
Stanford, CA 94305-2215

Principal Investigator: Amos Nur, 650 723-9526,
amos.nur@stanford.edu

Prepared for:
United States Department of Energy
National Energy Technology Laboratory

June 23, 2008

Office of Fossil Energy

DISCLAIMER

ABSTRACT

We quantify natural methane hydrate reservoirs by generating synthetic seismic traces and comparing them to real seismic data: if the synthetic matches the observed data, then the reservoir properties and conditions used in synthetic modeling might be the same as the actual, in-situ reservoir conditions. This approach is model-based: it uses rock physics equations that link the porosity and mineralogy of the host sediment, pressure, and hydrate saturation, and the resulting elastic-wave velocity and density. One result of such seismic forward modeling is a catalogue of seismic reflections of methane hydrate which can serve as a field guide to hydrate identification from real seismic data. We verify this approach using field data from know hydrate deposits.

TABLE OF CONTENTS

EXECUTIVE SUMMARY

We have developed an approach to natural methane hydrate quantification in which the user generates synthetic seismic traces and compares them to real seismic data. If the synthetic matches the observed seismogram, then the reservoir properties and conditions used in synthetic modeling might be the same as the actual, in-situ reservoir conditions. This methodology is based on rock physics equations that link (a) the porosity and mineralogy of the host sediment, pressure, and hydrate saturation, and (b) the resulting elastic-wave velocity and density. We have developed such rock physics equations that provide this link. One of them that appears essentially universal across various methane hydrate provinces is a model for unconsolidated sediment, where the hydrate acts as part of the mineral frame. This rock physics transform, combined with simple earth models, produces synthetic seismic reflections of gas hydrate that can be matched to real data and then perturbed to guide exploration and hydrate reservoir characterization. One result of such seismic forward modeling is a catalogue of seismic reflections of methane hydrate which can serve as a field guide to hydrate identification from real seismic data. The forward-modeling approach developed and advocated here results in non-unique solutions, because different combinations of rock properties may produce the same reflections. To constrain the spectrum of answers, the earth model used in the modeling has to be geologically-plausible, including ranges of porosity and clay content in the layers which are permissible within the hydrate stability window defined by the pore pressure and temperature. Such constraints are fairly straightforward to impose because most hydrate reservoirs of potential practical significance are high-porosity unconsolidated sands encased in unconsolidated shale. The configurations and spatial distributions of course may vary. The physics-based forward-modeling approach offered here is one way of addressing this natural diversity.

1. GENERAL PRINCIPLES

Seismic reflections depend on the contrast of the *P*- and *S*-wave velocity and density in the subsurface. Velocity and density, in turn, depend on lithology, porosity, pore fluid

and pressure. These two links, one between rock's structure and its elasticity and the other between the elasticity and signal propagation, form the physical basis of seismic interpretation for rock properties and subsurface conditions. One approach to interpreting seismic data for the physical state of rock is forward modeling. Lithology, porosity, and fluid in the rock, as well as the reservoir geometry, are varied and the corresponding elastic properties are calculated. Then synthetic seismic traces are generated. The underlying supposition is that if the seismic response is similar, the properties and conditions in the subsurface that give rise to this response are similar as well. Systematically conducted *perturbational forward modeling* helps create a catalogue of seismic signatures of lithology, porosity, and fluid away from well control and, by so doing, sets realistic expectations for hydrocarbon detection and optimizes the selection of seismic attributes in an anticipated depositional setting. The key to such perturbational forward modeling are rock physics-based relations between the lithology, mineralogy, texture, porosity, fluid, and stress in a reservoir and surrounding rock and their elastic-wave velocity and density. To this end, our goal is to develop and perfect methodologies of transforming geologically-plausible rock properties and conditions as well as reservoir and non-reservoir geometries into synthetic seismic traces and build a catalogue of synthetic *seismic reflections of rock properties*. Specific to the current application of this principle are *synthetic seismic reflections of methane hydrate*.

A common quantity that is calculated from reflection seismic data is acoustic impedance. By itself, acoustic impedance is virtually meaningless to the interpreter and engineer. Only after it is interpreted in terms of porosity, lithology, fluid, and pressure, can it be used to guide drilling decisions and reserve estimates. The problem with such interpretation is that one measured variable (in this case, the impedance) depends on several rock properties and conditions, including the total porosity, clay content, fluid compressibility and density, differential pressure, and rock-fabric texture. This means that often it is mathematically impossible to resolve this problem and predict rock properties from a seismic experiment. In other words, interpretation is non-unique, i.e., the same seismic anomaly may be produced by more than one combination of underlying rock properties.

A way to mitigate this non-uniqueness is to produce a catalogue of seismic signatures of rock properties and then distill the outcome by adding geologic constraints and site-specific knowledge of the subsurface under investigation. The question is how to systematically produce such a catalogue within a realistic physics-guided framework.

The traditional treatment of seismic data aims at obtaining a high-fidelity geometry of geobodies, their boundaries, and accompanying faults which makes possible a geologic interpretation for prospective hydrocarbon sources, migration conduits, traps, and seals. Seismic impedance inversion techniques allow us to look *inside* a geobody by mapping the elastic properties of its interior. The established approach to impedance inversion is the forward modeling of the seismic signatures of an earth model with an assumed spatial distribution of the velocity and density. The process starts with designing an initial earth model which is gradually perturbed to match synthetic seismograms with real data. Once this match is achieved (within a permissible accuracy tolerance) it is assumed that the underlying elastic earth model is the real one.

This methodology is illustrated in Figure 1.1 where the real seismic gather is displayed in the left-side track. To match this gather, a simple elastic earth model is created where a sand layer with the fixed *P*-wave velocity (V_p); the ratio of the *P*- to *S*-wave velocity (the V_p/V_s ratio); and bulk density (ρ_b) is inserted in shale with fixed elastic properties. Then a synthetic seismic gather is generated by numerically sending a wavelet of specified shape and frequency through this elastic-earth model.

Figure 1.1 indicates that the initial guess at the elastic properties of the subsurface did not result in a match between the synthetic and real gather. Next, we change the elastic properties of the sand layer by reducing its V_p, V_p/V_s, and ρ_b and thus arrive at a satisfactory match (Figure 1.2). Finally, we vary *both* the elastic properties of the shale and sand (Figure 1.3) and still arrive at a satisfactory match between the synthetic and real gathers. This latest example highlights the relative nature of the seismic amplitude: the same reflection can be produced by at least two different sets of absolute velocity and density values (Figure 1.3).

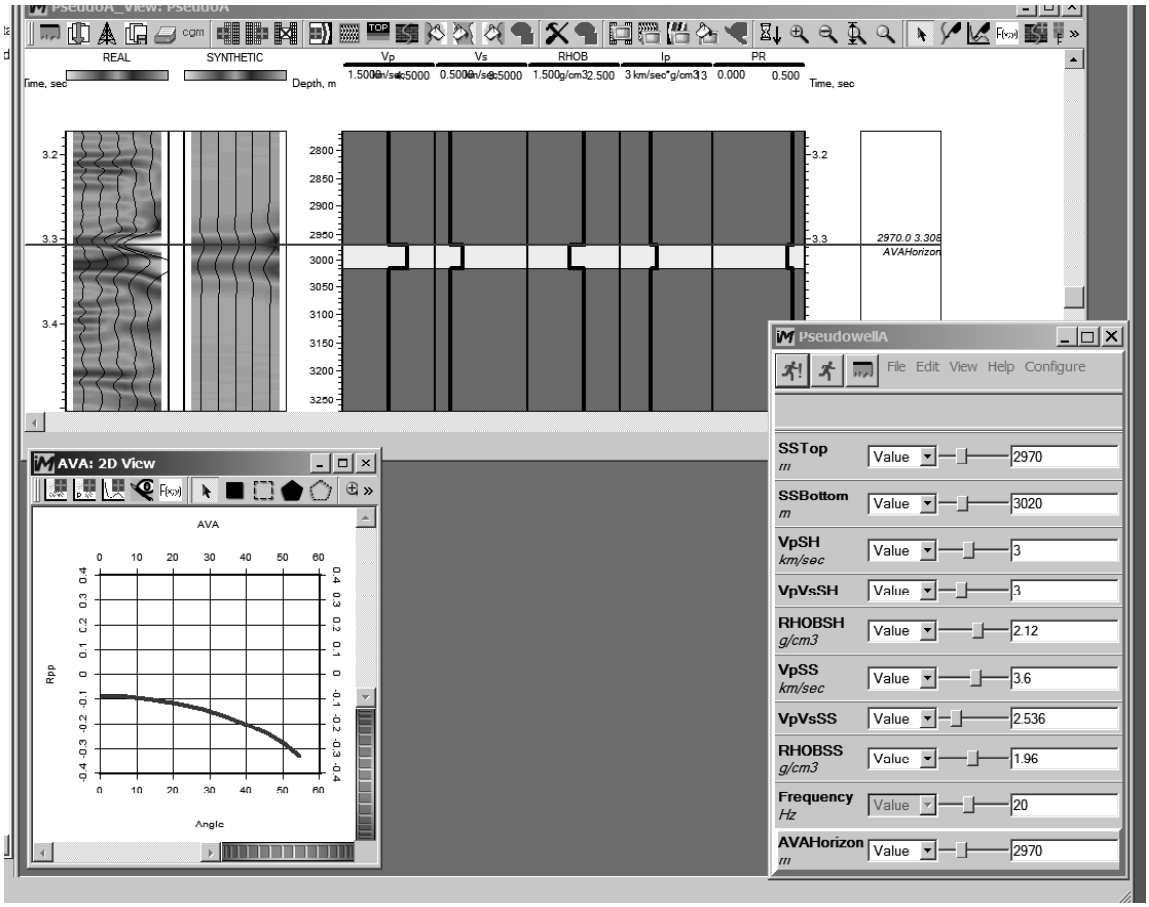

Figure 1.1. Real (left) and synthetic (right) seismogram gathers. The elastic earth model used to produce the latter is displayed in the tracks in the middle and listed in the dialogue box in the bottom-right corner. The frame in the bottom-left corner is the amplitude-versus-offset (AVO) readoff at the interface between shale and sand. In the seismic display, light and dark colors mark negative and positive amplitude, respectively.

To further elucidate the relative nature of the seismic amplitude, consider the simplest earth model which consists of two elastic half-spaces. The reflection is produced by the contrast of the elastic properties at the interface between these strata. The example in Figure 1.4 shows that the normal reflection is negative as a wave enters the lower half-space whose V_p as well as V_p/V_s are smaller than those in the upper half-space.

The amplitude of the reflection becomes increasingly negative as the angle of incidence of the wave (offset) increases. As we perturb the original earth model by reducing the velocity contrast between the two layers, the synthetic reflections become weaker (Figure 1.5). These reflections will completely disappear if the properties of the

layers become the same (or, in other words, the earth becomes elastically transparent).

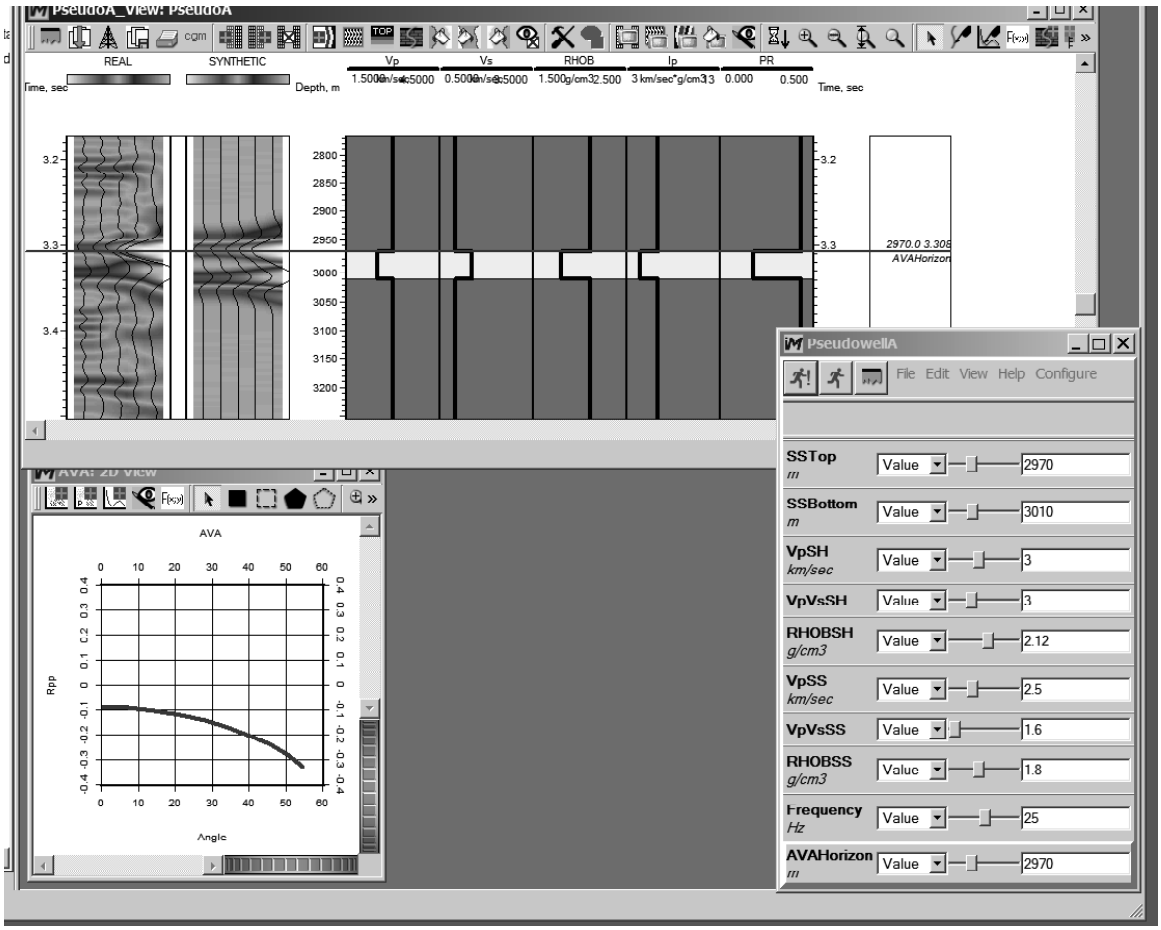

Figure 1.2. Same as Figure 1.1 but with different elastic properties of the sand layer.

Let us now fix the properties of the upper half-space and further reduce the velocity and density in the lower half-space. We observe that the reflection amplitudes rebound (Figure 1.6). They become essentially identical to these shown in Figure 1.4 although the underlying earth models are different.

This example once again underlines the dichotomy in geophysical remote sensing which is both relative and absolute: while the seismic reflection relates to the impedance contrast, the reservoir properties, such as porosity, relate to the absolute value of the impedance. One way of interpreting the relative in terms of the absolute is to perturb the absolute and calculate the corresponding relative.

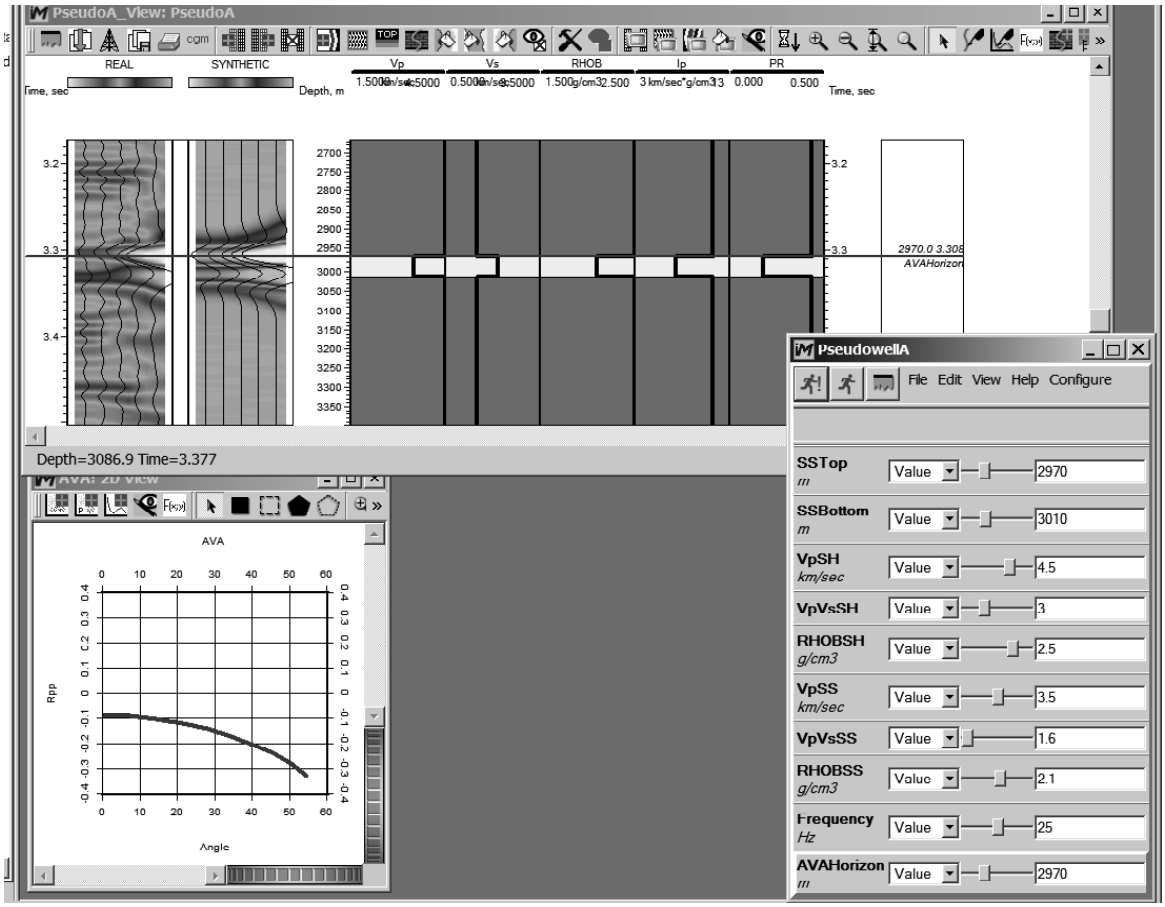

Figure 1.3. Same as Figure 1.2 but with different elastic properties of shale and sand.

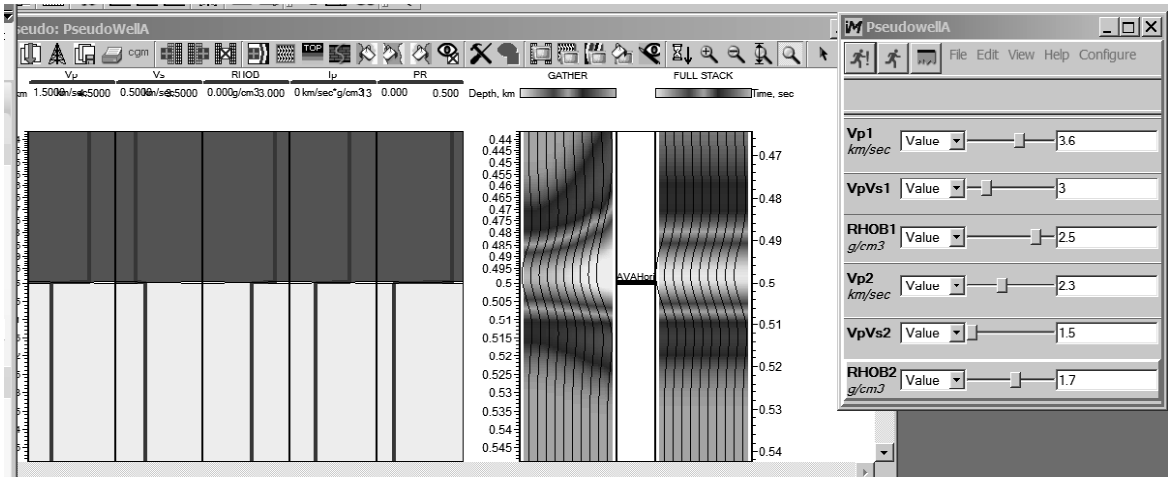

Figure 1.4. Synthetic seismogram (gather and full stack) at the interface between two elastic half-spaces with the properties specified in the box on the right side of the figure. These properties (velocity, density, P-wave impedance, and Poisson's ratio) are displayed in tracks on the left.

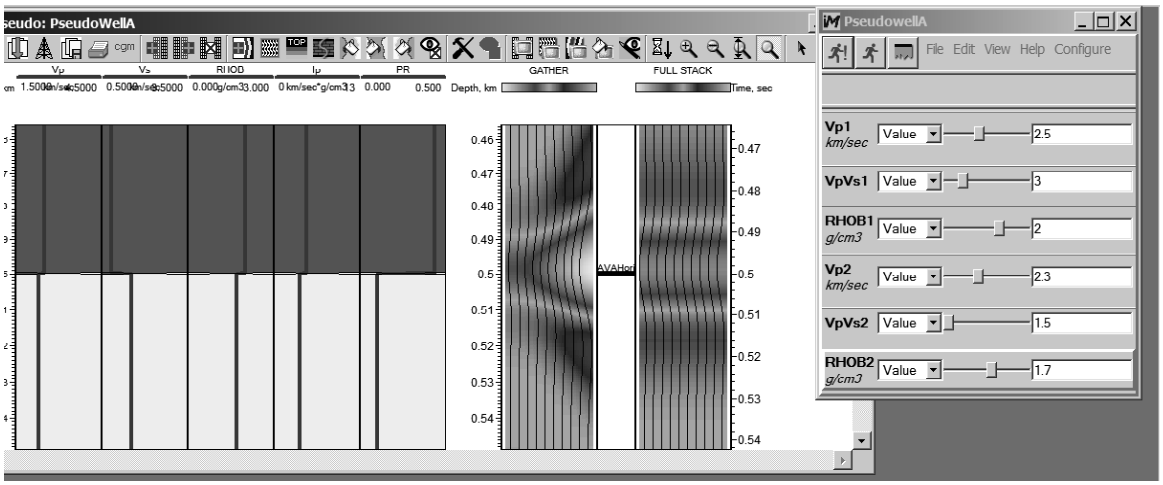

Figure 1.5. Same as Figure 1.4 but with smaller differences between the layers.

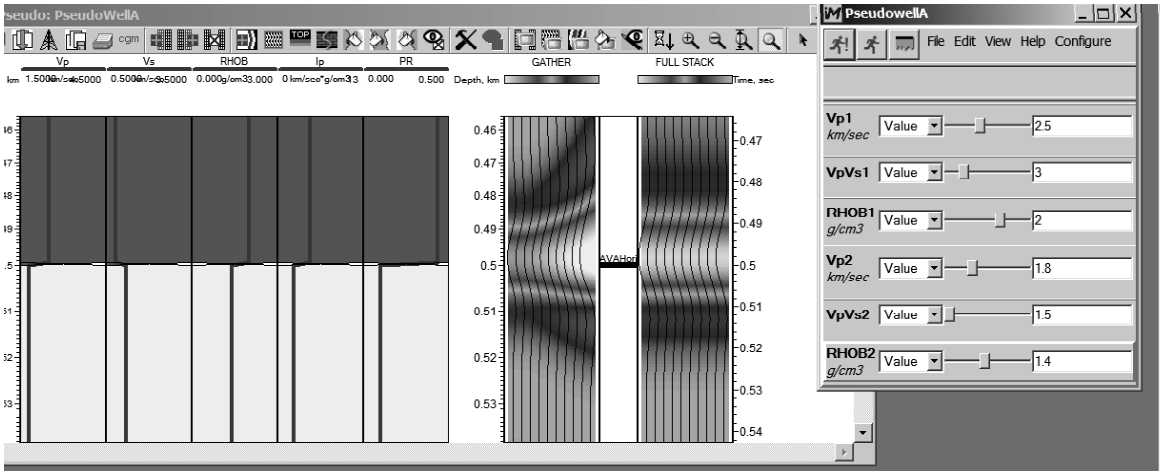

Figure 1.6. Same as Figure 1.5 but with reduced velocity and density in the lower layer.

Clearly, such interpretation is not unique. Different earth models can produce the same response. In traditional impedance inversion, this non-uniqueness is mitigated by anchoring the elastic properties to a nearby well. Once an absolute impedance map is available, an impedance-porosity, impedance-lithology, and/or impedance-fluid transform can be applied to it to map these reservoir properties. One of such transforms is shown in Figure 1.7 for a sandstone dataset.

Still, even if a perfect impedance map of the subsurface is available and an appropriate transforms have been established, their application to seismic impedance may not be straightforward because usually such transforms are obtained at the laboratory or well log scale (inch or ft), while seismic impedance maps have the seismic scale which is

much larger (hundreds of feet). This means that seismic interpretation for rock properties is never unique. This non-uniqueness comes from at least two sources: (a) the scale disparity between the traditional rock physics and seismic scales; and (b) the relative versus absolute disparity between the seismic reflection and actual physical impedance.

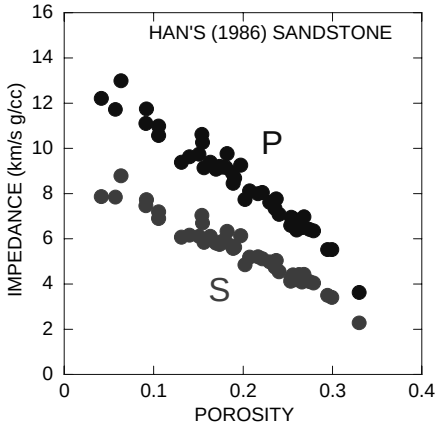

Figure 1.7. P- and S-wave impedance versus porosity for gas-saturated low-clay-content sandstone samples.

Therefore, we need to admit that it might be impossible to obtain uniquely the physical properties of the subsurface to match real seismic data. To mitigate this fact we may aspire to produce a set of variants that do so and then narrow the search by using geologic and petrophysical knowledge and selecting only the variants that are plausible and reasonable. For example, in reference to Figure 1.6, one may argue that the velocity selected for the sand layer is too small and unlikely to occur within the depth range relevant to the problem. Then this variant is rejected and only the one shown in Figure 1.4 is accepted. This acceptance criterion is much more reasonable to design in the space of the bulk properties of rock, such as porosity and mineralogy, and conditions, such as saturation and pressure, than in the elastic property space. This is why our next task is to perturb the bulk properties and conditions and, by so doing, arrive at a synthetic-to-real seismogram match.

The example used in Figure 1.1 is now shown in Figure 1.8 but with porosity, clay content, and water saturation now assigned to shale and sand. In this initial trial we fail to obtain the desired match. Next, we add gas to the sand layer (Figure 1.9) and, by so doing, improve the match. By reducing the water saturation from 0.8 to 0.2 we obtain

even better match (Figure 1.10).

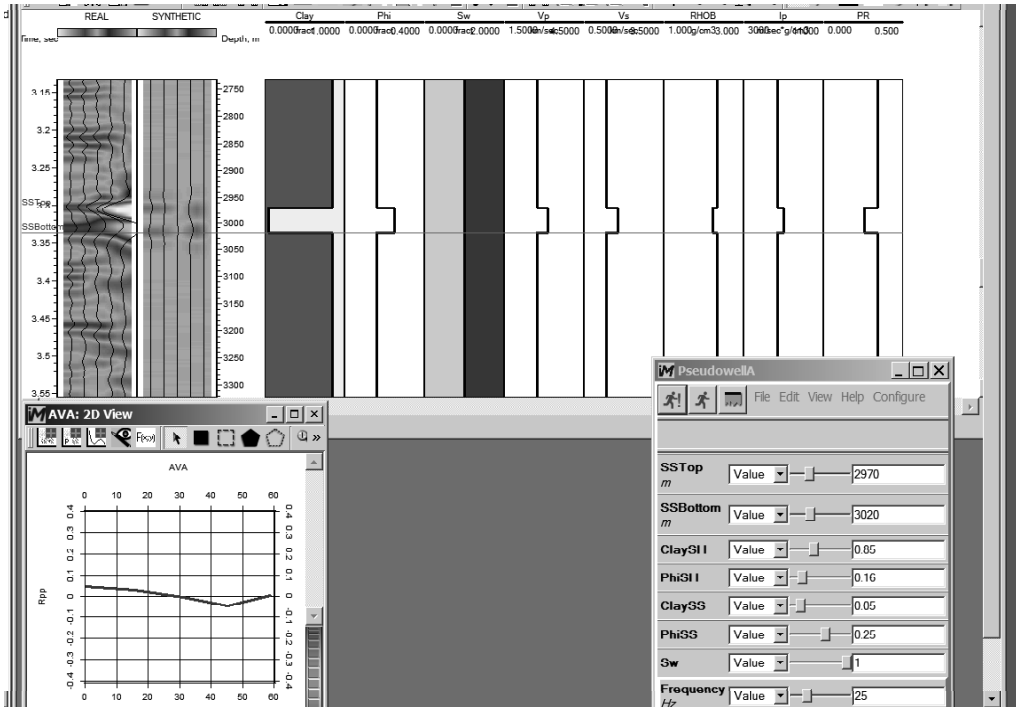

Figure 1.8. Same as Figure 1.1 but with porosity, clay content, and saturation assigned to the earth model.

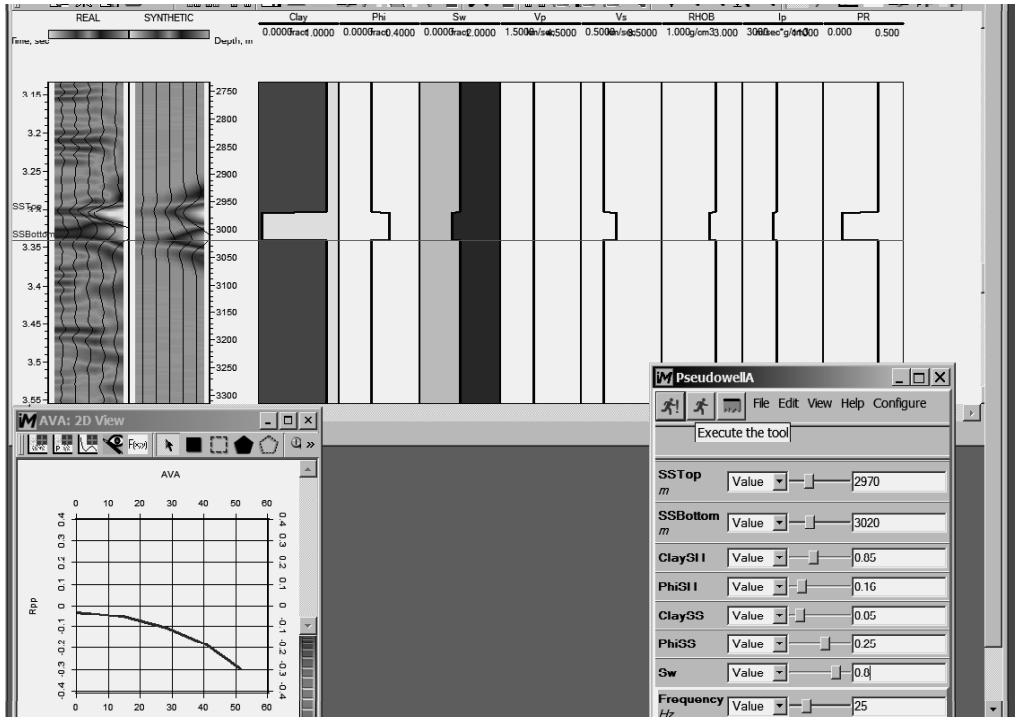

Figure 1.9. Same as Figure 1.8 but with gas in the sand.

Instead of stopping our search at this successful attempt, we can now proceed by embarking upon a "what-if" search. In the example in Figure 1.11 we increase the porosity in the shale thus making it less compacted than in the previous examples. The match deteriorates. To restore the match we can, e.g., increase the porosity in the sand as well thus making it highly uncompacted (Figure 1.12). This is arguably a dubious success because it once again indicates that two different pairs of the shale and sand properties produce almost the same seismic response.

Yet, in spite of this non-uniqueness, we argue that it is much easier for the geologist and petrophysicist to select a plausible and realistic variant while perturbing porosity, clay content, and saturation than doing so with velocity and density.

The engine hidden behind the images in Figures 1.9 to 1.12 is a rock physics transform similar to that shown in Figure 1.7. Such a transform is key to this approach to synthetic-seismic modeling and, eventually, correct determination of reservoir properties responsible for the observed seismic amplitude. The methodology of obtaining such a transform is *rock physics diagnostics*.

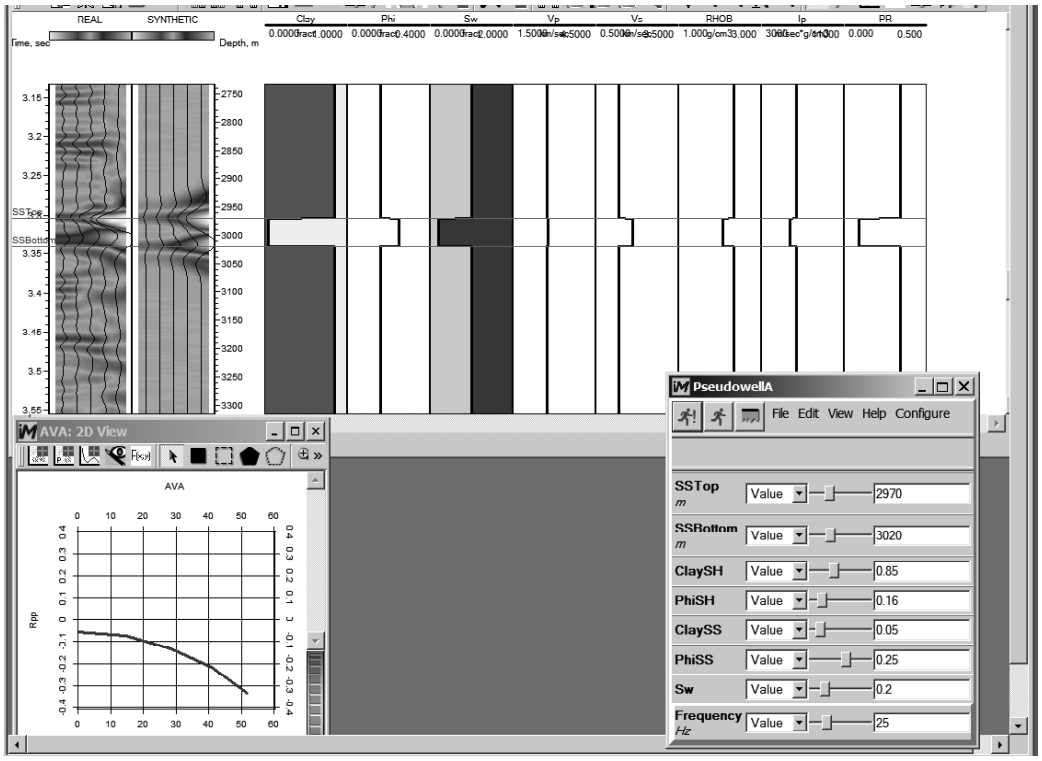

Figure 1.10. Same as Figure 1.9 but with further reduced water saturation in the sand.

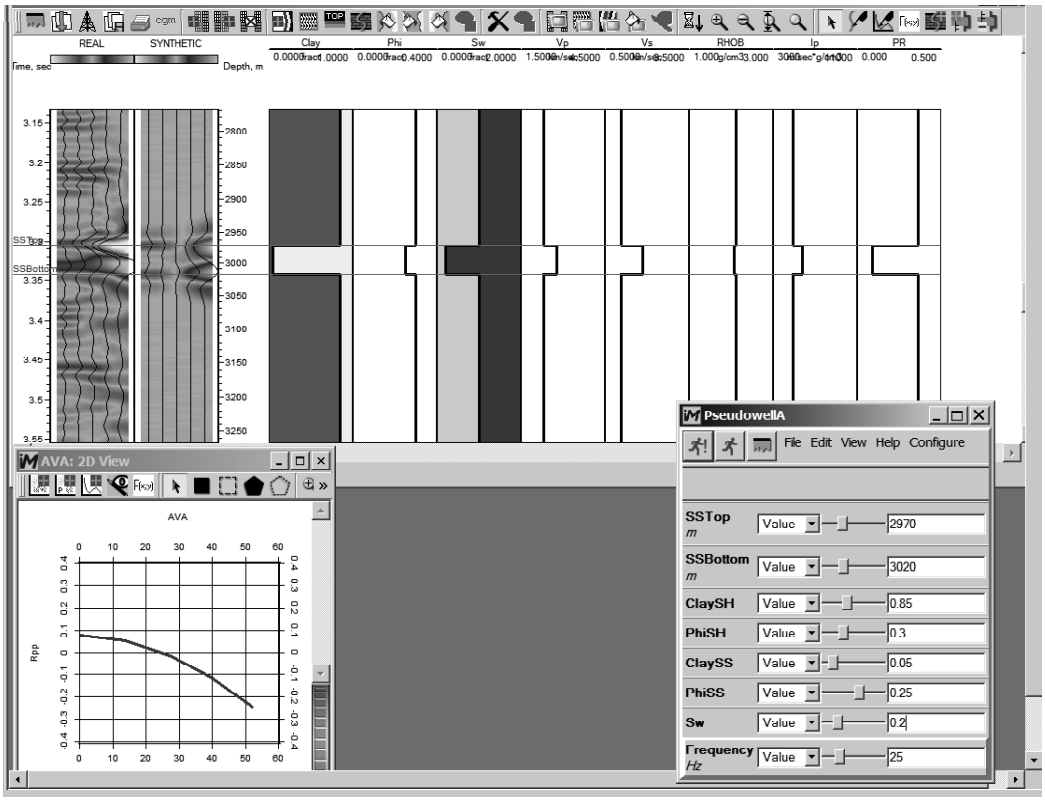

Figure 1.11. Same as Figure 1.9 but with changed properties of the shale.

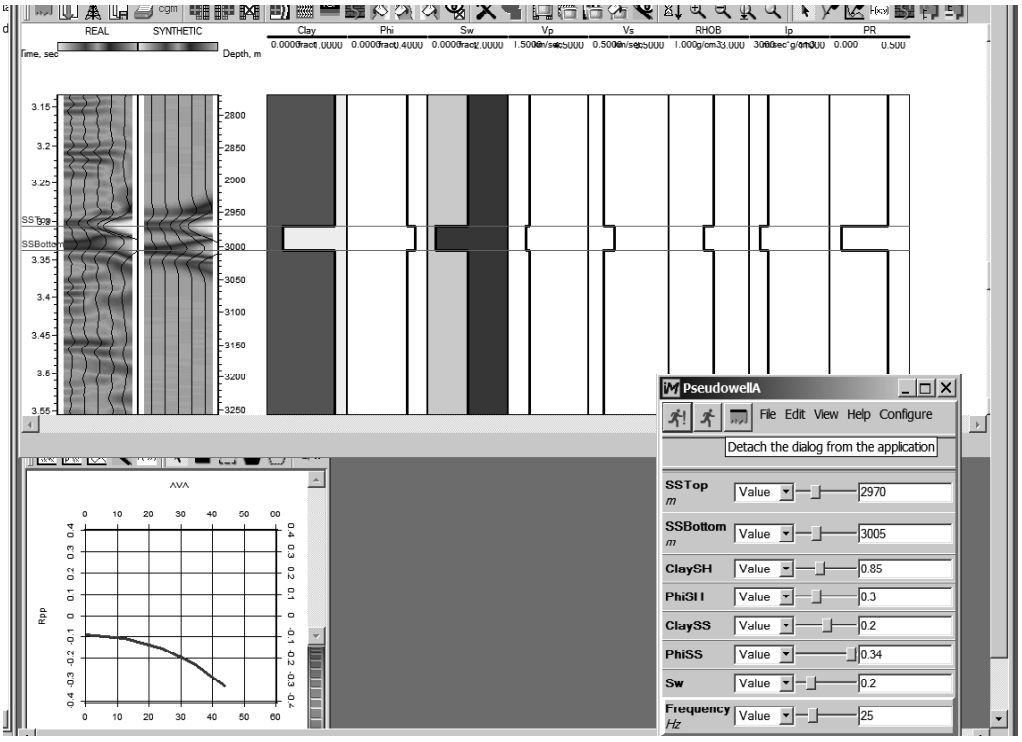

Figure 1.12. Same as Figure 1.11 but with increased porosity of the sand.

Rock physics diagnostics is a process of matching the in-situ, observed trends through available rock physics models. Typically, to uncover the effects of porosity and clay on the velocity, we first bring the data to the *common fluid denominator* by theoretically substituting the in-situ pore fluid with the formation brine throughout the well and calculating the corresponding elastic properties and density. This fluid substitution is needed to reduce by one the number of variables that affect the elastic-wave velocity and bulk density by balancing the pore-fluid effect in the well.

Rock physics diagnostics is a deterministic process. Physics-based determinism is usually accepted with more confidence than blind statistical fitting simply because extrapolating a statistical trend outside the range of the data used or exporting the trend into a different geographical location and depositional setting may be invalid and risky. A deterministic rock physics model can be either empirical or effective-medium-based. The critical requirement for a model is that it be *predictive*.

For example, an inclusion-based theoretical model where the aspect ratio of the inclusions or aspect ratio distribution between various mineral components have to be changed every time a new dataset is encountered *is not* predictive. Conversely, a model based on extensive empirical material that has been systematically confirmed by new data years after it was proposed *is* predictive. Below we will discuss a number of such models and show that one of them, designed to describe unconsolidated granular sediment where hydrate acts as part of the mineral matrix, is fit to link the bulk properties and conditions of hydrate-bearing sand to the sediment's elastic properties.

A note on terminology: a rock physics *conceptual model* is a hypothesis of how the mineral matrix, pore fluid, and methane hydrate are positioned in the pore space; this conceptual model is used to derived a corresponding *mathematical model*, which, in turn, results in *rock physics equations*.

2. APPLICATION TO METHANE HYDRATE RESERVOIRS

Gas hydrates are solids where gas molecules are locked inside cage-like structures of hydrogen-bonded water molecules. The physical properties of hydrates are remarkably close to those of pure ice. According to Helgerud (2001), the *P*- and *S*-wave velocity in

methane hydrate may reach 3.60 and 1.90 km/s, respectively, while its density is 0.910 g/cc. The corresponding values for ice are 3.89 and 1.97 km/s, and 0.917 g/cc, respectively. As a result, sediment with hydrate in the pore space, similar to frozen earth, is much more rigid than sediment filled solely by water.

However, unlike ice, methane hydrate can be ignited. A unit volume of hydrate releases about 160 unit volumes of methane (under normal conditions). Also, unlike ice, hydrate can exist at temperatures above 0^o C, but not at room conditions -- it requires high pore pressure to form and remain stable.

Such stability conditions are present on the deep shelf: high pressure is supported by the thick water column while the temperature remains fairly low (but above 0^o C) at depths of several hundred feet below the seafloor because temperature increase with depth starts at a low level, just a few degrees Celsius at the bottom of the ocean. Hydrates also exist onshore below the permafrost which acts to lower temperature at depth where the hydrostatic pressure is already high. Of course, favorable pressure and temperature are necessary but not sufficient for hydrate formation. Its molecular components, water and gas, have to be available at the same place and time.

Once all of these conditions are in place, and hydrate forms, the elevated rigidity of sediment with hydrate makes it discernable in a seismic reflection volume. Relatively high *P*-wave impedance of this sediment stands out in the low-impedance background of shallow and unconsolidated deposits. Its seismic response is a reflection which runs parallel to the seafloor, the so-called bottom-simulating reflector (BSR). Free gas, which is sometimes trapped underneath the hydrate-filled host sediment, enhances this reflection, often changes its character, and adds an amplitude-versus-offset (AVO) effect. The presence of gas hydrate (which is a dielectric) in the pore space is also revealed by increased electrical resistivity and, therefore, may be remotely detected by an electromagnetic survey.

BSR's are abundant in the ocean. Measurements from dozens of research wells directly confirm that these reflections are due to methane hydrate. Onshore drilling in Canada, Alaska, and Siberia has also revealed the widespread extent of methane hydrate in these Arctic regions. Seasonal hydrate mounds have been visually detected on the

bottom of the Gulf of Mexico and at other offshore sites. These discoveries indicate that natural hydrates may constitute a gigantic, untapped pool of methane resource.

The implications for society are at least threefold: (1) a natural hydrate reservoir can serve as a source of fuel; (2) temporal variations in sea level and earth temperature may act to release methane from destabilized hydrate and vent it into the ocean and atmosphere which, in turn, may affect the global climate; and (3) sediment with hydrate, similar to permafrost, can become a geohazard if disturbed by engineering activity. These factors drive scientific and industrial interest in understanding and quantifying methane hydrate in the subsurface, mainly by means of geophysical remote sensing.

Gas hydrate quantification is, in principle, no different from traditional hydrocarbon reservoir characterization. Similar and well-developed remote sensing techniques can be used, seismic reflection profiling being dominant among them.

Thus a question is: What properties and conditions of a methane hydrate reservoir and surrounding sediment can produce the observed seismic reflection?

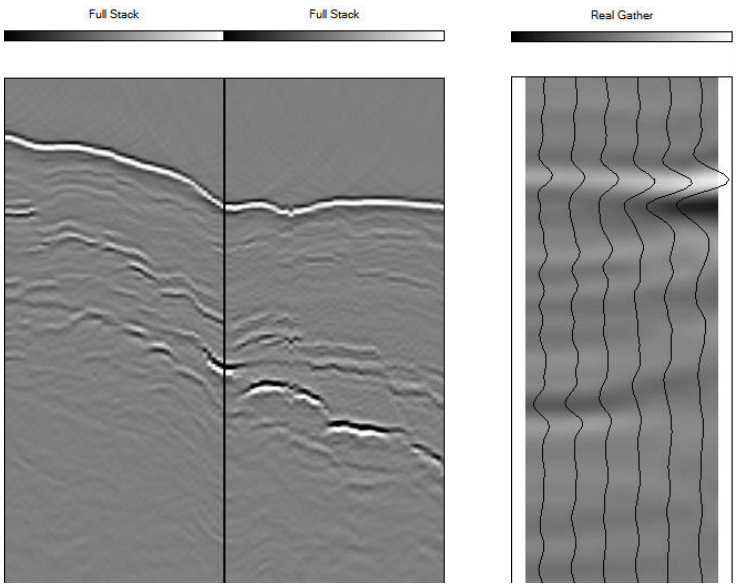

Figure 2.1. Seismic sections at methane hydrate reservoirs. Left – full-offset stack at the Hydrate Ridge offshore Oregon with the seafloor and hydrate reflections (courtesy Nathan Bangs, UT Austin). Right – a single gather at a hydrate reservoir at another offshore location. Light color indicates positive amplitude (peak) while dark is for negative amplitude (trough).

Seismic response of the subsurface (Figure 2.1) is determined by the spatial

distribution of the elastic properties. The elastic properties depend on porosity, lithology, texture, and hydrate content. These two links connect seismic response to the desired reservoir properties and condition, namely porosity and hydrate saturation of the pore space. Our approach to addressing the question posed is: (a) create a geologically plausible earth model; (b) assign porosity, mineralogy, and hydrate saturation to the layers in this model; (c) calculate the *P*- and *S*-wave velocity and density from porosity, mineralogy, and hydrate saturation; (d) generate synthetic seismic traces using these elastic parameters; and (e) match this synthetic seismogram to the real data.

The key hypothesis that underpins this approach is that if synthetic traces match real traces, the properties and conditions in the subsurface used to produce the former are similar to the actual properties and conditions that produced the latter.

The key element of this approach is relating porosity, mineralogy, stress, and hydrate saturation to the elastic properties of the sediment. One way of achieving this goal is through rock physics effective-medium modeling.

3. ROCK PHYSICS MODELS IN PERSPECTIVE

Rock physics was initiated several decades ago as a "velocity-porosity" discipline. Arguably the first transform between porosity and velocity was introduced by Wyllie et al. (1956) as the famous time average equation (WTA). It states that the total travel time through rock is the volume-weighted sum of the travel times through the solid phase and the fluid phase considered independently of each other, i.e., $V_p^{-1} = (1-\phi)V_{pS}^{-1} + \phi V_{pF}^{-1}$, where ϕ is the total porosity, V_p is the P-wave velocity in the rock, and V_{pS} and V_{pF} are the P-wave velocity in the solid and in the pore-fluid phases, respectively.

The work of Wyllie et al. (1956) was based on laboratory measurements of ultrasonic wave propagation through a pile of alternating Lucite and aluminum disks set parallel to one another. The individual disk thickness varied between 1/16 and 1/2 inch. As expected, the total travel time through such a layered system was the sum of the travel times through Lucite and aluminum considered independently of each other. By examining a large dataset of artificial and natural liquid-saturated porous samples, Wyllie et al. (1956) established the remarkable and somewhat unexpected fact that the velocity

data can be approximately described by the time average, as if the mineral grains and the pore space in rock were arranged in relatively thick layers normal to the direction of wave propagation.

Obviously, this is not what the pore structure of many natural sediments appears to be, which means that Wyllie's time average is a useful and simple but physically deceptive way of summarizing extensive experimental data (as acknowledged by the authors of this equation in the original publication). Therefore, further exploiting this equation by summing up travel times through the mineral components of the solid phase and/or through the components of the pore-filling material (water and gas hydrate) cannot be justified by first-principle physics and thus is likely to be erroneous.

Another velocity-porosity transform widely used in petrophysical analyses is by Raymer et al. (1980). It is a purely empirical equation originally designed for water-saturated sediment: $V_p = (1-\phi)^2 V_{pS} + \phi V_{pF}$ (RHG). Spikes and Dvorkin (2005) show that this equation is Gassmann-consistent, which means that it can be applied to rock with any fluid as long as V_{pF} is assigned a consistent value, including perfectly dry rock where V_{pF} = 0. Clearly, WTA is not Gassmann-consistent because it fails at V_{pF} = 0.

In Figure 3.1 we show velocity-porosity cross-plots for three laboratory datasets where the velocity was measured using the ultrasonic pulse transmission technique. In the first dataset, Han (1986) used consolidated mature sandstone samples. In the second dataset, Strandenes (1991) used high-porosity sand from the Oseberg field in the North Sea whose grains were cemented at their contacts. In the third one, Blangy (1992) used high-porosity unconsolidated and friable sand from the Troll field in the North Sea. All samples selected here contained no or very small amounts of clay. The dry-rock velocity obtained at 20 MPa confining pressure was used as the starting point and the wet-rock velocity was calculated by Gassmann's (1951) fluid substitution for water with bulk modulus 2.33 GPa and density 1.03 g/cc.

Superimposed upon these data are RHG and WTA model curves. Both models provide accurate estimates of the measured velocity in consolidated samples as well as contact-cemented samples. However, both RHG and WTA overestimate the velocity in unconsolidated North Sea and Ottawa sand.

A velocity-porosity transform appropriate for a suspension of solid grains in fluid by Wood (1955) states that the bulk modulus of the sediment is the harmonic average of those of the components (the shear modulus of a suspension is zero), and the density is the arithmetic average of those of the components. The velocity is the square root of the modulus divided by density. This curve is also plotted in Figure 3.1. It strongly underestimates the data.

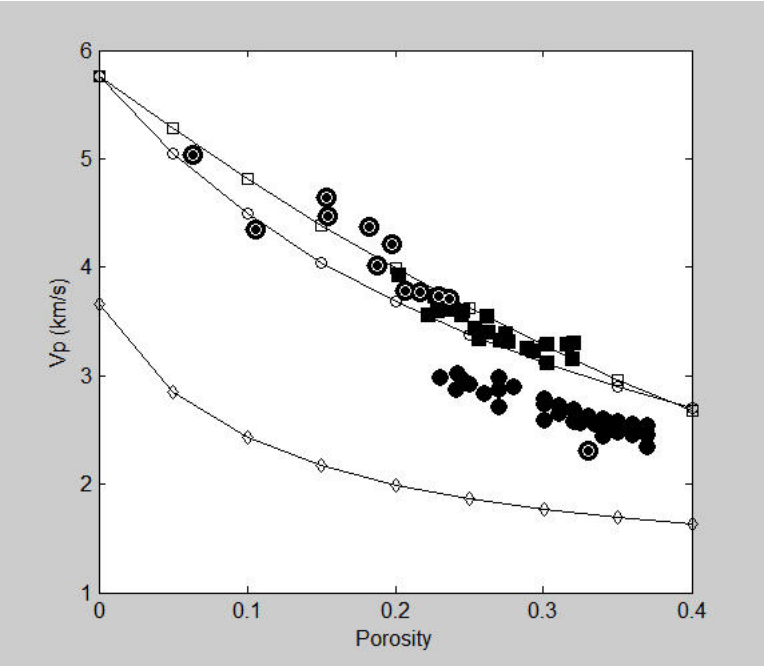

Figure 3.1. The *P*-wave velocity in wet rock versus porosity. Black circles with white rim inside are for Han's (1986) data. Solid squares are for the Strandenes (1991) data. Solid circles are for the Blangy (1992) data. Han's (1986) high-porosity data point comes from unconsolidated Ottawa sand. The curve punctuated by squares is for RHG. The curve punctuated by circles is for WTA. The lower curve punctuated by diamonds is for Wood's (1941) equation. All model curves are calculated for water-saturated sediment with 0.95 quartz and 0.05 clay mineralogy.

Clearly, neither WTA nor RHG work in unconsolidated sediment (see also Schlumberger, 1989; Dvorkin and Nur, 1998), where most of methane hydrate is concentrated. Wood's (1941) suspension model is also inappropriate for such rock.

Nevertheless, various modifications of WTA as well as weighted combinations of WTA and the suspension model have found their way into gas hydrate characterization literature (Pearson et al., 1983; Miller et al., 1991; Bangs et al., 1993; Scholl and Hart,

1993; Minshull et al., 1994; Wood et al., 1994; Holbrook et al., 1996; Lee, 2002). Generally, by fine-tuning the input parameters and weights, these equations can be forced to fit a selected dataset. The problem with such fitting is that equations not based on first physical principles provide little or no physical insight. More important, *they are not predictive*, because it is difficult to establish a rational pattern of adapting free model parameters to site-specific conditions during exploration.

Nonetheless, it is instructive to mention here that all existing rock physics models *can*, in principle, be used to simulate the presence of hydrate in sediment. To accomplish this, we will assume that (a) the hydrate mechanically acts as part of the mineral matrix and, conversely, (b) it acts as part of the pore fluid. Assume, along these lines, that the total porosity of sediment is ϕ_t while the hydrate saturation in the pore space is S_h. The remainder of the pore space is filled with water. The porosity available to water is $\phi_t(1-S_h)$. This liquid-bearing porosity will be used below in the WTA and RHG models to provide an example of using these models for estimating the elastic properties of a methane hydrate reservoir.

In this example, we consider sand with porosity 0.35 and clay content 0.05, filled with water whose bulk modulus is 2.65 GPa and density 1 g/cc. The velocity versus hydrate saturation is shown in Figure 3.2 for hydrate being part of the mineral matrix (left) and part of the pore fluid (right). The relevance of the latter case to methane hydrate reservoirs can be immediately ruled out because extensive observations indicate that both P- and S-wave velocity increase with increasing hydrate content. However, the hydrate being part of pore fluid does not seemingly affect the S-wave velocity according to RHG. The relevance of the former case is also questionable because the P-wave velocity in high-porosity sand with hydrate usually does not exceed 4 km/s even at a very high hydrate content.

The first breakthrough in the rock physics of gas hydrate was due to Hyndman and Spence (1992). They constructed an empirical relation between porosity and velocity for sediment without gas hydrate and approximated the effect of hydrate presence on sediment velocity by a simple reduction in porosity. By doing so, they effectively assumed that hydrate becomes part of the frame without altering the frame's elastic

properties.

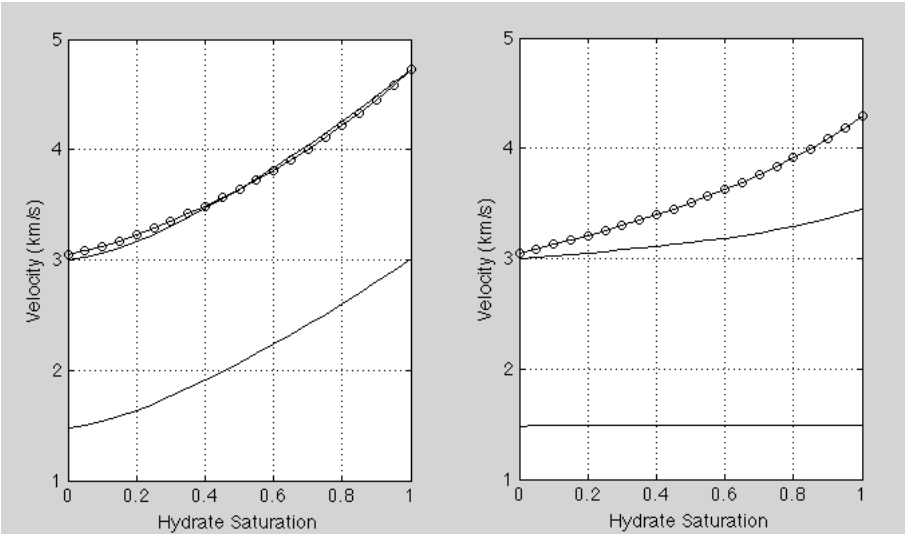

Figure 3.2. Velocity versus hydrate saturation in sand (example in the text with reference to this figure). Left – hydrate is part of the mineral matrix. Right – hydrate is part of the pore fluid. Solid lines are for RHG while open symbols connected by solid lines are for WTA. WTA does not provide S-wave velocity prediction.

Helgerud et al. (1999) further developed this idea by using a physics-based effective-medium model to quantify methane hydrate concentration from sonic and check-shot data in a well drilled through a large offshore methane hydrate reservoir at the Outer Blake Ridge in the Atlantic. Sakai (1999) used this model to accurately predict methane hydrate concentration from well log *P*- and *S*-wave as well as VSP data in an on-shore gas hydrate well in the Mackenzie Delta in Canada. Ecker et al. (2000) used the same model to successfully delineate gas hydrates and map their concentration at the Outer Blake Ridge from seismic interval velocity.

This effective-medium model still includes free parameters, e.g., the coordination number (the average number of grain-to-grain contacts per grain). Nevertheless, these free parameters have a clear physical meaning and ranges of variation as opposed to weight coefficients applied to ad-hoc selected equations in order to reconcile a model with data. A physical effective-medium model properly adopted to reflect the nature of the sediment under examination is *predictive* simply because its parameters can be selected in a rational and consistent way to honor the site-specific conditions, such as the

effective stress, clay content, and degree of consolidation.

Essentially all of discovered natural methane hydrate is concentrated in clastic and highly unconsolidated reservoirs, either offshore or on-shore. To honor this fact we will concentrate on effective-medium models that are relevant to the nature and texture of such sediment.

4. EFFECTIVE-MEDIUM MODELS FOR HIGH-POROSITY CLASTICS

The effective-medium models discussed here determine first the bulk and shear elastic moduli of an isotropic *dry-frame* (K_{Dry} and G_{Dry}, respectively), and then use them to calculate the moduli of the sediment saturated with fluid (K_{Sat} and G_{Sat}) via Gassmann's (1951) *fluid substitution*:

$$K_{Sat} = K_s \frac{\phi K_{Dry} - (1+\phi) K_f K_{Dry}/K_s + K_f}{(1-\phi) K_f + \phi K_s - K_f K_{Dry}/K_s}, \quad G_{Sat} = G_{Dry}, \tag{4.1}$$

where K_s, and K_f are the bulk moduli of the solid phase and pore-fluid, respectively, and ϕ is the total porosity.

The bulk density (ρ_b) is obtained from mass balance:

$$\rho_b = (1-\phi)\rho_s + \phi\rho_f, \tag{4.2}$$

where the density of the solid (mineral) phase is $\rho_s = (1-C)\rho_q + C\rho_c$ and ρ_f is the density of the pore fluid. Here we assume that the sediment has only two mineral components, quartz and clay (with volume content in the solid phase C), whose densities are ρ_q and ρ_c, respectively.

The elastic-wave velocities (V_p and V_s) relate to the elastic moduli (K and G) and density (ρ) as

$$M = \rho V_p^2, \quad G = \rho V_s^2, \quad K = M - \tfrac{4}{3} G, \tag{4.3}$$

where M is the compressional modulus.

An alternative to Equation (4.1) is the Mavko et al. (1995) approximate *P*-wave only fluid substitution method:

$$M_{Sat} = M_s \frac{\phi M_{Dry} - (1+\phi) K_f M_{Dry} / M_s + K_f}{(1-\phi) K_f + \phi M_s - K_f M_{Dry} / M_s}, \tag{4.4}$$

where the compressional modulus M replaces the bulk modulus K in Gassmann's (1951) equation (for fluid M and K are the same). Equation (4.4) is useful for fluid substitution on field data where V_s is not available or reliable.

The initial building block of the *dry frame* is a random dense pack of elastic spherical grains which represents well-sorted sand at its maximum porosity, the critical porosity ϕ_c, which in sand may vary between 0.35 and 0.45 (Nur et al., 1998).

The effective elastic bulk (K_{HM}) and shear (G_{HM}) moduli of this isotropic pack are

$$K_{HM} = \frac{n(1-\phi_c)}{12\pi R} S_N, \quad G_{HM} = \frac{n(1-\phi_c)}{20\pi R} (S_N + \frac{3}{2} S_T), \tag{4.5}$$

where n is the coordination number (the average number of contacts per grain), R is the average radius of the grain, and S_N and S_T are the normal and tangential stiffnesses, respectively, between two grains in contact (e.g., Dvorkin, 1996).

The coordination number n in a sphere pack at critical porosity is about 6 (e.g., Dvorkin and Nur, 1996). The stiffnesses S_N and S_T are defined as the proportionality coefficients between the relative displacements (normal U_N and tangential U_T, respectively) and the reaction forces (F_N and F_T, respectively) for two individual grains in contact (Figure 4.1):

$$F_N = S_N U_N, \quad F_T = S_T U_T. \tag{4.6}$$

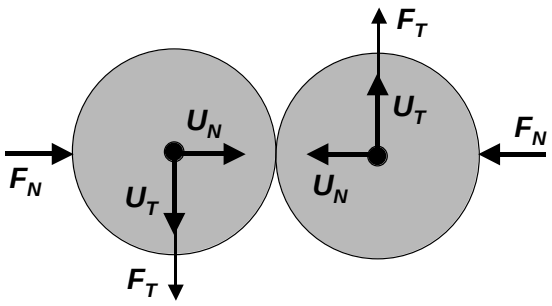

Figure 4.1. Two individual spherical grains in contact. The normal and tangential displacements are shown as bold arrows while the forces are fine arrows.

Equation (4.5) shows that the contact stiffnesses directly affect the elastic moduli of a

grain pack. These stiffnesses, in turn, depend on the character of the contact, specifically on whether the grains are cemented at the contact or kept together merely by the confining stress. At the same porosity, grain aggregates with cemented contacts may be much stiffer (at the same porosity) than those without cement (e.g., Dvorkin et al., 1994). Let us concentrate on the latter situation.

The contact stiffnesses of a pair of elastic spheres with strong friction at the contact (perfect adhesion) are (Mindlin, 1949):

$$S_N = \frac{4aG_s}{1-\nu_s}, \quad S_T = \frac{8aG_s}{2-\nu_s}, \tag{4.7}$$

where a is the radius of the circular contact area between the spheres and G_s and ν_s are the shear modulus and Poisson's ratio of the material of the grains, respectively. a is zero when no external normal forces are applied to the spheres. It monotonically increases as these forces increase.

The normal force F_N between two spheres is related to the hydrostatic confining stress P applied to the aggregate as (e.g., Mavko et al., 1998)

$$F_N = \frac{4\pi R^2 P}{n(1-\phi_c)}. \tag{4.8}$$

The radius of the contact area is

$$a = \left[F_N \frac{3(1-\nu_s)}{8G_s} R \right]^{\frac{1}{3}} = R \left[\frac{3\pi(1-\nu_s)}{2n(1-\phi_c)G_s} P \right]^{\frac{1}{3}}. \tag{4.9}$$

Equations (4.5), (4.7), and (4.9) provide the expressions for K_{HM} and G_{HM}:

$$K_{HM} = \left[\frac{n^2(1-\phi_c)^2 G_s^2}{18\pi^2(1-\nu_s)^2} P \right]^{\frac{1}{3}}, \quad G_{HM} = \frac{5-4\nu_s}{5(2-\nu_s)} \left[\frac{3n^2(1-\phi_c)^2 G_s^2}{2\pi^2(1-\nu_s)^2} P \right]^{\frac{1}{3}}. \tag{4.10}$$

For frictionless spheres, S_T = 0 while S_N is the same as in the case of perfect adhesion. As a result, Equations (4.5) become

$$K_{HM} = \frac{n(1-\phi_c)}{12\pi R} S_N, \quad G_{HM} = \frac{n(1-\phi_c)}{20\pi R} S_N, \quad \frac{K_{HM}}{G_{HM}} = \frac{5}{3}, \tag{4.11}$$

which means that the Poisson's ratio of the dry frame of a frictionless sphere pack (ν_{HM}) is constant, no matter which material the grains are made of:

$$\nu_{HM} = \frac{1}{2}\frac{(V_p/V_s)^2 - 2}{(V_p/V_s)^2 - 1} = \frac{1}{2}\left(1 - \frac{3}{3K_{HM}/G_{HM} + 1}\right) = 0.25. \tag{4.12}$$

It is not constant, however, for particles with perfect adhesion:

$$\frac{K_{HM}}{G_{HM}} = \frac{5(2-\nu_s)}{3(5-4\nu_s)}, \quad \nu_{HM} = \frac{\nu_s}{2(5-3\nu_s)}. \tag{4.13}$$

There is a large difference between the Poisson's ratio of a dry frictionless pack and a dry pack with perfect adhesion between the particles (Figure 4.2). In the latter case, ν_{HM} does not exceed 0.1 no matter what material the grains are made of.

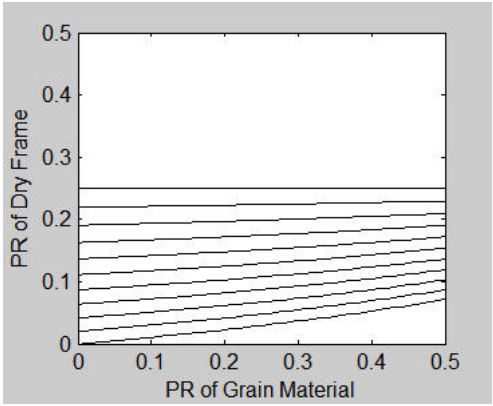

Figure 4.2. Poisson's ratio of a grain pack versus that of the grain material. The upper curve is according to Equation (4.12) while the lower one is according to Equation (4.13). The intermediate curves are according to Equation (4.15) with f varying between 0 (upper curve) and 1 (lower curve) with step 0.1.

Let us assume that part of the individual contacts are frictionless, i.e., $S_T = 0$, while the rest have perfect adhesion, i.e., $S_T = 8aG_s/(2-\nu_s)$. To quantify this assumption, we introduce an *ad-hoc* coefficient f $(0 \le f \le 1)$ such that

$$S_N = \frac{4aG_s}{1-\nu_s}, \quad S_T = f\frac{8aG_s}{2-\nu_s}. \tag{4.14}$$

This equation replaces Equation (7) and implies that as f increases from 0 to 1, the number of frictionless contacts decreases from the total number of all contacts to zero.

By combining Equations (4.5) and (4.14) we obtain

$$K_{HM} = \left[\frac{n^2(1-\phi_c)^2 G_s^2}{18\pi^2(1-\nu_s)^2} P\right]^{\frac{1}{3}},$$
$$G_{HM} = \frac{2+3f-\nu_s(1+3f)}{5(2-\nu_s)}\left[\frac{3n^2(1-\phi_c)^2 G_s^2}{2\pi^2(1-\nu_s)^2} P\right]^{\frac{1}{3}}, \qquad (4.15)$$
$$\nu_{HM} = \frac{2-2f+\nu_s(2f-1)}{2[4+f-\nu_s(2+f)]}.$$

As f varies between 0 and 1, ν_{HM} gradually moves from the frictionless line down to the perfect-adhesion curve (Figure 4.2).

The model described by Equations (4.15) is applicable to a grain pack at the critical porosity thus providing the elastic moduli at this high-porosity endpoint. The other endpoint is at zero porosity where the elastic moduli and density of the sediment are those of the mineral phase. They can be calculated from the properties of the components according to the Hill (1952) average and mass balance:

$$K_s = 0.5\cdot\left[\sum_{i=1}^{m} f_i K_i + \left(\sum_{i=1}^{m} f_i / K_i\right)^{-1}\right], \quad G_s = 0.5\cdot\left[\sum_{i=1}^{m} f_i G_i + \left(\sum_{i=1}^{m} f_i / G_i\right)^{-1}\right],$$
$$\rho_s = \sum_{i=1}^{m} f_i \rho_i, \qquad (4.17)$$

where K_s, G_s, and ρ_s are the bulk and shear moduli and density of the mineral (solid) phase, respectively; m is the number of the mineral components; f_i is the volumetric fraction of the i-th component in the solid phase; K_i, G_i, and ρ_i are the bulk and shear moduli and density of the i-th component, respectively.

The next question is how to connect these two endpoints in the elastic moduli versus porosity plane. These trajectories depend on the process that governs porosity reduction. Dvorkin and Nur (1996) discuss two modes of the pore-space geometry alteration that give rise to the same porosity reduction down from the critical porosity. One mode is the cementation of the grains where cement envelops the original grains and by so doing reduces the total porosity. The other mode is pore-filling where small particles fill the pore space reducing the total porosity in the process ("uncemented" or "soft" sand).

The first, cementing, mode strongly affects the grain-to-grain contacts by reinforcing

them with additional material. The resulting increase in the elastic moduli and velocity is very large even if the porosity reduction is small (Figure 4.3). The second, pore-filling, mode does not strongly affect the grain-to-grain contacts although it still acts to reduce porosity. The resulting increase in the elastic moduli and velocity is relatively modest (Figure 4.3).

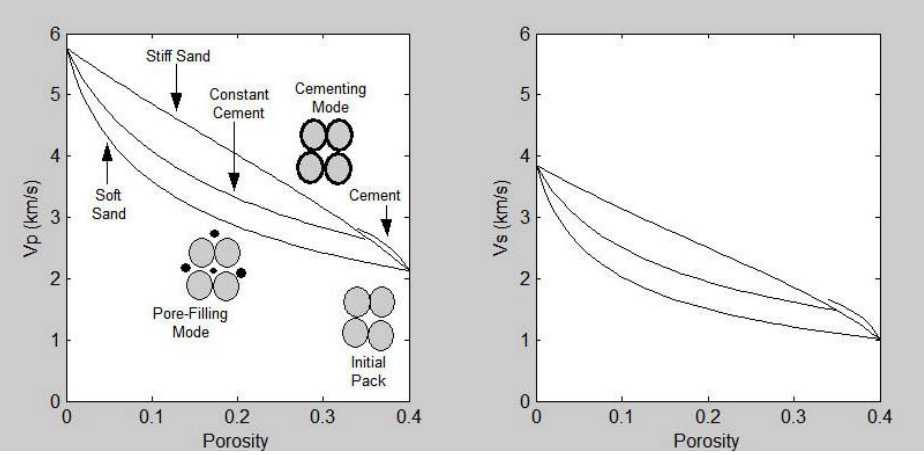

Figure 4.3. *P*- (left) and *S*-wave velocity (right) versus porosity for four modes of porosity reduction. All model curves are calculated for water-saturated sediment with 0.95 quartz and 0.05 clay mineralogy.

An intermediate (or combined) mode is the "constant cement" mode (Avseth et al., 2000). In this case, the grain pack is initially cemented to a certain degree after which cement deposition stops and the following porosity reduction is by pore-space filling. Porous systems of the same porosity and identical mineralogy may have drastically different velocity depending on the type of the grain-to-grain contacts.

We concentrate here on the uncemented (or "soft-sand") model which is of special interest in methane hydrate exploration. The two end-points are connected by curves that have the functional form of the lower Hashin-Shtrikman bound (Dvorkin and Nur, 1996):

$$K_{Dry} = \left[\frac{\phi/\phi_c}{K_{HM} + \frac{4}{3}G_{HM}} + \frac{1-\phi/\phi_c}{K_s + \frac{4}{3}G_{HM}}\right]^{-1} - \frac{4}{3}G_{HM},$$
$$G_{Dry} = \left[\frac{\phi/\phi_c}{G_{HM} + Z} + \frac{1-\phi/\phi_c}{G_s + Z}\right]^{-1} - Z, \quad Z = \frac{G_{HM}}{6}\left(\frac{9K_{HM} + 8G_{HM}}{K_{HM} + 2G_{HM}}\right). \tag{4.18}$$

The constant-cement model is essentially the same model but with the high-porosity end-

point lying on the cement-model curve (Figure 4.3).

A counterpart set of equations is the "stiff-sand" equations which use the same end-points but, instead of using the lower Hashin-Shtrikman bound functional form to connect these end-points, it employs the upper Hashin-Shtrikman bound (Figure 4.3):

$$K_{Dry} = \left[\frac{\phi/\phi_c}{K_{HM} + \frac{4}{3}G_s} + \frac{1-\phi/\phi_c}{K_s + \frac{4}{3}G_s}\right]^{-1} - \frac{4}{3}G_s,$$
$$G_{Dry} = \left[\frac{\phi/\phi_c}{G_{HM} + Z} + \frac{1-\phi/\phi_c}{G_s + Z}\right]^{-1} - Z, \quad Z = \frac{G_s}{6}\left(\frac{9K_s + 8G_s}{K_s + 2G_s}\right). \tag{4.19}$$

An example from an offshore well penetrating clastic sediment is shown in Figure 4.4. Here, the clean-sand branches of the velocity-porosity data are matched by constant-cement curves calculated for the 100%-quartz mineralogy. At the same time, the shaley clay-rich parts are bounded underneath by soft-sand curves calculated for the 100%-clay mineralogy. The soft-sand curves for the 100%-quartz mineralogy underestimate the velocity measured in clean sand. In this well we simultaneously encounter partially-cemented sand and completely unconsolidated shale.

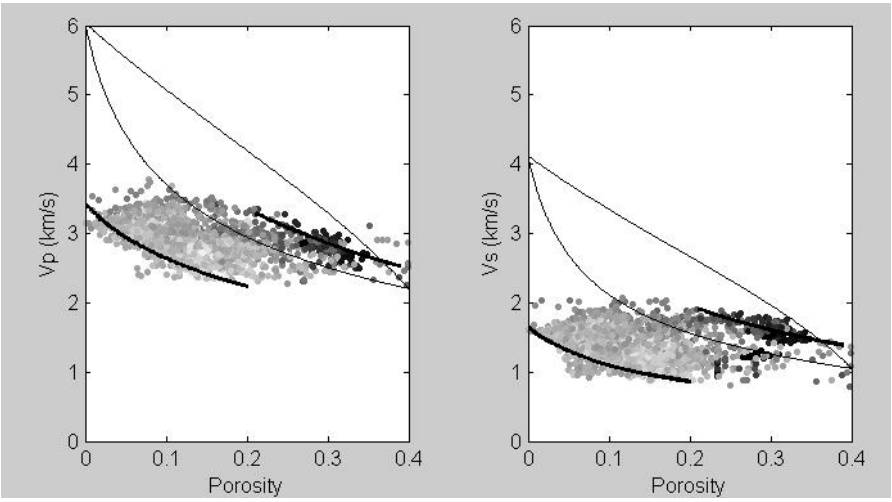

Figure 4.4. *P*- (left) and *S*-wave velocity (right) versus porosity from an offshore well, color-coded by gamma-ray (GR). Dark is for low GR (clean sand) while light is for high GR (clay-rich sediment). The upper bold curves are from the constant-cement model (100% quartz). The lower bold curves are from the soft-sand model (100% clay). The fine curves that lie below the black-colored data points are from the soft-sand model (100% quartz). The fine curves that lie above these data points are from the stiff-sand model (100% quartz).

A different rock physics model that examines a reservoir where pure-hydrate inclusions are dispersed in hydrate-free sediment is presented in Appendix III.

5. MODELING EXAMPLE

All of the above models (contact cement, constant cement, soft sand, and stiff sand) can be directly applied to sediment with gas hydrate by assuming that the hydrate becomes part of the mineral frame. To quantify this effect, we need to introduce the hydrate saturation of the pore space S_h which is the ratio of the hydrate volume in a unit volume of rock to the total porosity of the original mineral frame ϕ_t. The volumetric concentration of hydrate in a unit volume of rock C_h is $\phi_t S_h$. The total porosity of sediment with hydrate ($\overline{\phi}$) where hydrate is considered part of the mineral phase is

$$\overline{\phi} = \phi_t - C_h = \phi_t(1 - S_h). \tag{5.1}$$

$\overline{\phi}$ becomes ϕ_t for S_h = 0 and zero for S_h = 1.

The volume fraction of hydrate in the new solid phase that includes the hydrate is $C_h/(1-\overline{\phi}) = \phi_t S_h/[1-\phi_t(1-S_h)]$. The volume fraction of the i-th constituent in the host sediment's solid phase in the new solid phase is $f_i(1-\phi_t)/(1-\overline{\phi}) = f_i(1-\phi_t)/[1-\phi_t(1-S_h)]$. The elastic moduli and density of the new solid phase material that includes hydrate can be calculated now according to Equations (4.17) but using these new volume fractions instead of the original f_i and adding the hydrate.

A different approach to modeling the elastic properties of sediment with hydrate is to assume that the hydrate is suspended in the brine and thus acts to change the bulk modulus of the pore fluid without altering the elastic moduli of the mineral frame. In this case, the total porosity of the mineral frame does not change and remains ϕ_t. The bulk modulus of the pore fluid that is now a mixture of brine and hydrate ($\overline{K}_f$) is the harmonic average of those of hydrate (K_h) and brine (K_f):

$$\overline{K}_f = \left[S_h/K_h + (1-S_h)/K_f\right]^{-1}, \tag{5.2}$$

while its density ($\overline{\rho}_f$) is the arithmetic average of those of hydrate (ρ_h) and brine (ρ_f):

$$\overline{\rho}_f = S_h \rho_h + (1 - S_h)\rho_f . \tag{5.3}$$

The shear modulus of the sediment with gas hydrate remains unchanged, the same as it was in the wet sediment without hydrate. The bulk modulus is calculated from Gassmann's equation (4.1) but with $\overline{K}_f$ used instead of K_f. The bulk density ρ_b is $\rho_s(1-\phi_t) + \overline{\rho}_f \phi_t$.

Consider now a high-porosity sand pack. The pore space of this pack is filled with brine. The methane hydrate that we place in the pore space replaces part of the brine. Let us explore three types of hydrate arrangement in the pores (Figure 5.1): (a) hydrate acts as contact cement – the cemented-sand (or stiff-sand) model; (b) hydrate acts as a pore-filling component of the mineral frame – the soft-sand model; and (c) hydrate is suspended in the brine without mechanically interacting with the mineral frame.

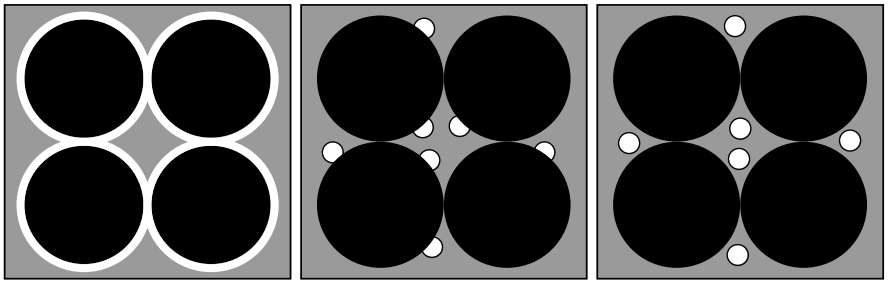

Figure 5.1. Three types of methane hydrate arrangement in the pore space. From left to right – (a) hydrate as contact cement; (b) non-cementing hydrate as part of the mineral frame; and (c) hydrate as part of the pore fluid. The mineral grains are black; brine is gray; and hydrate is white.

The results of calculating the elastic-wave velocity using these three models are shown in Figure 5.2 where data from methane hydrate exploratory wells at the Mallik site (e.g., Dvorkin and Uden, 2004) are displayed as well. Apparently, model "b" in which the hydrate is a non-cementing component of the mineral frame matches the data best. Some of the data points fall above and below this model curve, which may mean that small parts of hydrate act as contact cement at the grain contacts as well as being suspended in the pore fluid (assuming that the data are correct and internally consistent).

The elastic moduli and densities of the components of sediment with methane hydrate used in this example are listed in Table 5.1. The properties of the hydrate are from Helgerud (2001). Those of quartz, clay, and calcite are from Mavko et al. (1998).

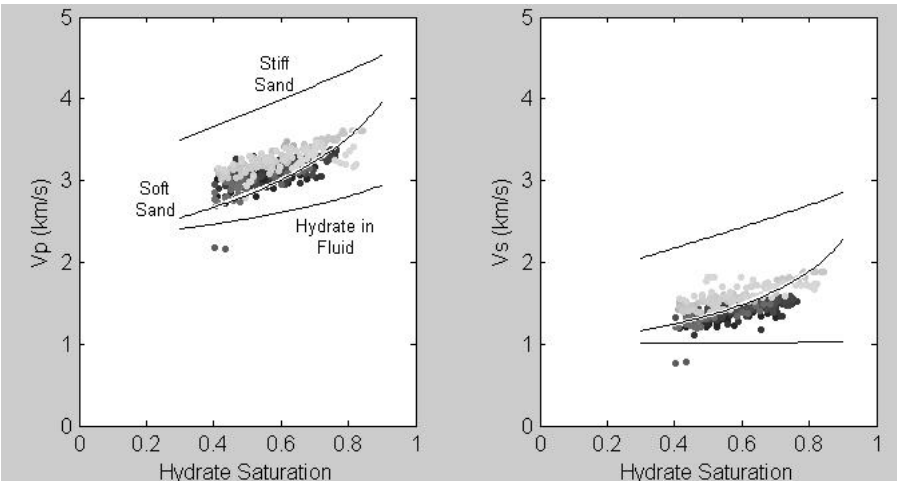

Figure 5.2. *P*- and *S*-wave velocity versus methane hydrate saturation in a quartz-sand-brine-hydrate system. The upper curves are from the stiff-sand model. The lower curves are from the hydrate-in-fluid model. The middle curves are from the soft-sand model. The symbols are log data from a methane hydrate well Mallik-2L-38. The data are color-coded by depth where light is for deep and dark is for shallow. The model curves are calculated with parameters relevant to the shallow-depth portion of the well.

Table 5.1. Elastic moduli and densities of rock and fluid components.

Component	Bulk Modulus (GPa)	Shear Modulus (GPa)	Density (g/cc)
Quartz	36.60	45.00	2.650
Clay	21.00	7.00	2.580
Calcite	76.80	32.00	2.710
Methane Hydrate	7.40	3.30	0.910
Brine	2.330	0.00	1.029
Gas	0.017	0.00	0.112

Another strong argument in favor of using model "b" is that field data typically indicate that both *P*- and *S*-wave velocity increase with increasing methane hydrate saturation. This fact helps us refute model "c" because if methane hydrate is assumed to be part of the pore fluid, no increase of the *S*-wave velocity due to the presence of hydrate in the pore space can be theoretically obtained.

Essentially, all previous hydrate-related studies using these effective-medium models to mimic field log and seismic data (Helgerud et al., 1999; Sakai, 1999; Ecker et al., 2000; Dvorkin et al. 2003; Dvorkin et al., 2003; Dai et al., 2004) arrived at the same conclusion.

Comparative modeling results (using this soft-sand model) for the elastic properties of sand with methane hydrate and gas as well as shale are shown in Figure 5.3. The porosity of the hydrate sand varies in the 0.2 to 0.4 range and hydrate saturation is in the zero to 1.0 range. The clay content in this sand is selected zero and 0.4. In the sand with hydrate, the velocity and impedance slightly decrease with the increasing clay content while Poisson's ratio decreases.

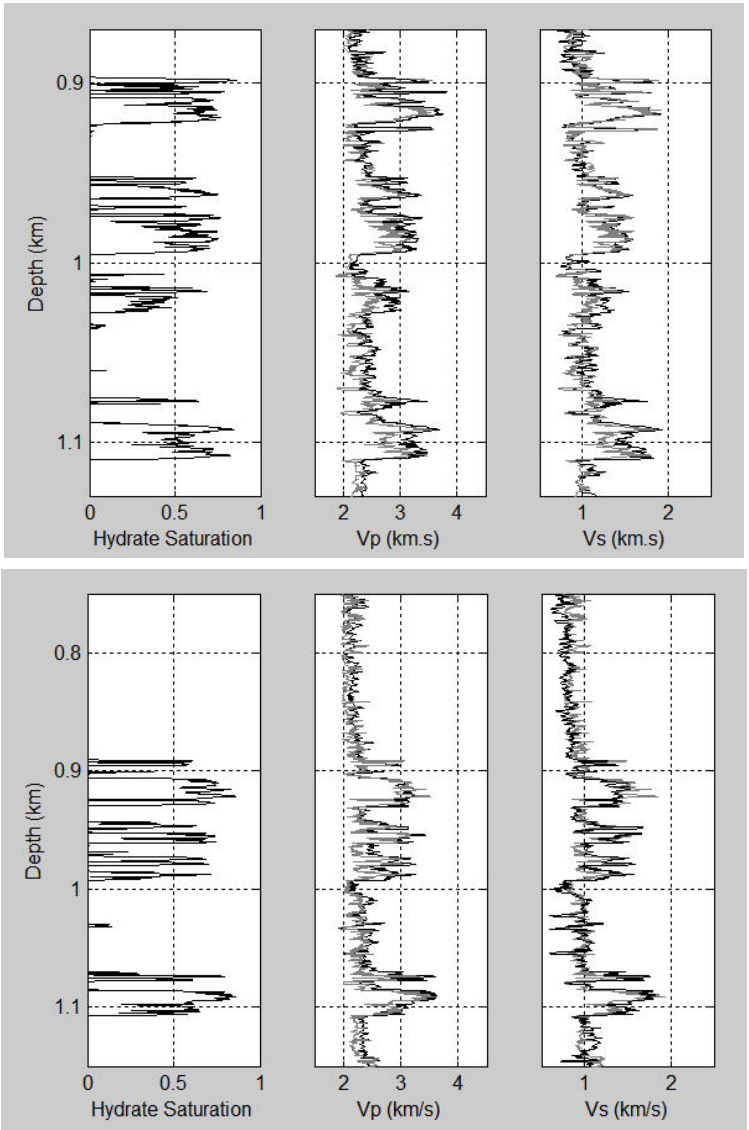

Figure 5.3. Mallik well 2L-38 (top) and 5L-38 (bottom) depth curves. From left to right – hydrate saturation as calculated from resistivity (Cordon et al., 2006); the *P*-wave velocity measured (black) and calculated (gray) using model (b); and the *S*-wave velocity measured (black) and calculated (gray) using model (b).

The same "hydrate-part-of-mineral-frame" approach can be used with any rock physics model, including WTA and RHG. To do so we need to assume certain initial porosity of the host sediment and then theoretically mix hydrate with the original minerals to obtain the *P*- and *S*-wave velocity of this new solid mix.

The original RHG equation is only for V_p. Here we add an ad-hoc RHG equation for V_s by assuming that in dry sediment $V_{sDry} = (1-\phi)^2 V_{sS}$, where V_{sS} is the S-wave velocity in the solid phase. V_s in the wet sediment is obtained from V_{sDry} by assuming that the rock's shear modulus is not affected by pore fluid:

$$V_s = V_{sDry}\sqrt{\frac{\rho_{bDry}}{\rho_b}} = (1-\phi)^2 V_{sS}\sqrt{\frac{(1-\phi)\rho_s}{(1-\phi)\rho_s + \phi\rho_f}}, \tag{5.4}$$

where ρ_{bDry} and ρ_b is the bulk density of dry and wet sediment, respectively; and ρ_s and ρ_f is the density of the solid and fluid phase, respectively.

These equations can be tested to match and explain new field measurements. However, they are not appropriate for any of the existing data where the soft-sand model appears to serve the best (see examples in Section 2, Figure 2.3).

6. APPLICATION TO WELL DATA: VERIFICATION OF MODEL

Dvorkin and Uden (2004) and Cordon et al. (2006) applied model "b" discussed in the previous section to data from on-shore exploratory methane hydrate wells at the Mallik site. The model accurately delineates the sands with hydrate from water-saturated sand and shale without hydrate (Figure 6.1).

Another display of these modeling results is given in Figure 6.2 where the velocity is plotted versus the porosity of the mineral frame (without methane hydrate) and color-coded by the hydrate saturation of the pore space. The model curves superimposed upon these data are from model (b) and calculated in a porosity range for wet clean sand without methane hydrate and also for hydrate saturation 0.4 and 0.8. These model curves are consistent with the measured velocity.

The next field example is for the ODP well 995 at the Outer Blake Ridge (Helgerud et al., 1999; Ecker et al., 2000). The sediment at this location is very different from that at the Mallik site: it is predominantly clay with noticeable amounts of calcite and small

quantity of quartz. Helgerud et al. (1999) assumed for modeling purposes uniform mineralogy of 5% quartz, 35% calcite, and 60% clay. The porosity of the mineral frame (without gas hydrate) was that measured on the core material. The hydrate saturation was calculated from resistivity.

The sonic velocity is compared to the soft-sand model predictions in Figure 6.3. The latter reproduces the measurement, except for the upper part where the resistivity indicates the presence of hydrate while the sonic velocity remains low. We cannot explain this inconsistency in the data.

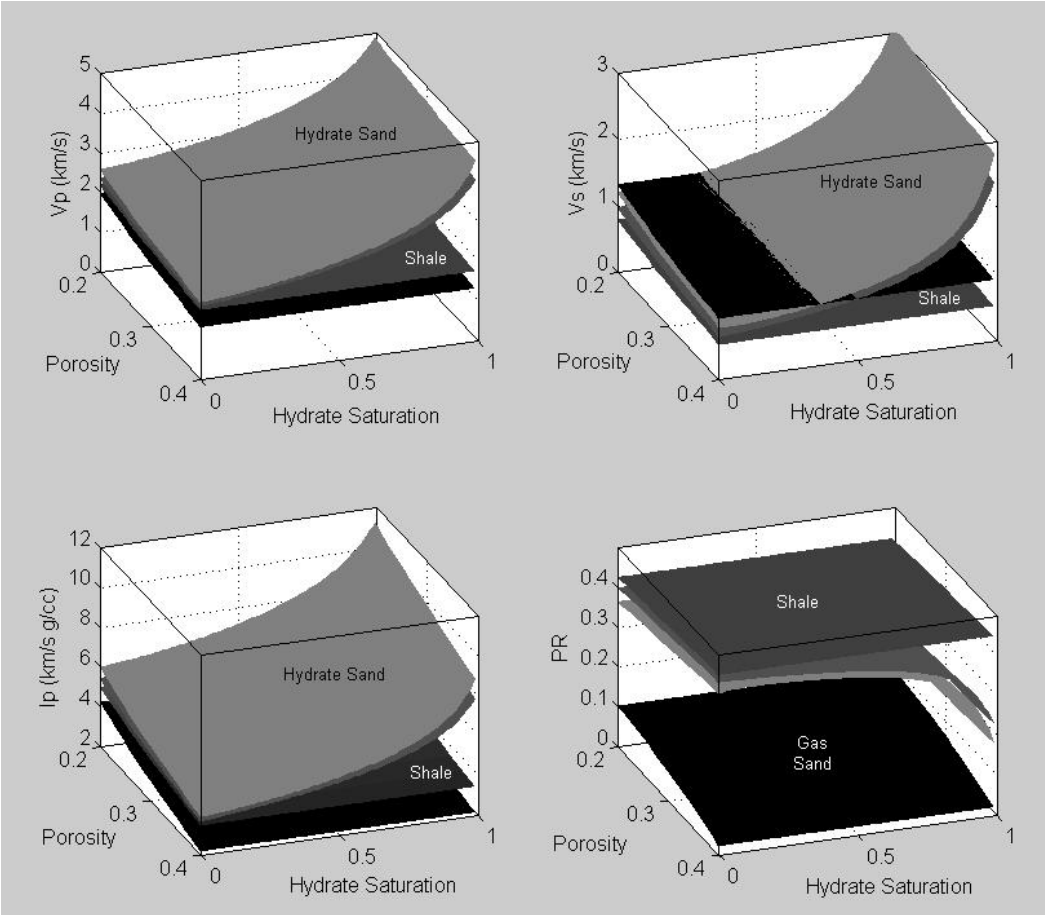

Figure 6.1. *P*- and *S*-wave velocity (top row) and acoustic impedance and Poisson's ratio (bottom) of sand with zero and 0.4 clay content versus the porosity of the host sand and methane hydrate saturation of the pore space. Also displayed are these elastic properties of shale with clay content 0.8 and gas sand (30% gas saturation) with zero clay content. Color-coding is by the vertical axis value. Gas sand is shown in black; shale in dark-gray; and hydrate sand in light-gray (zero clay) and darker gray (0.4 clay content).

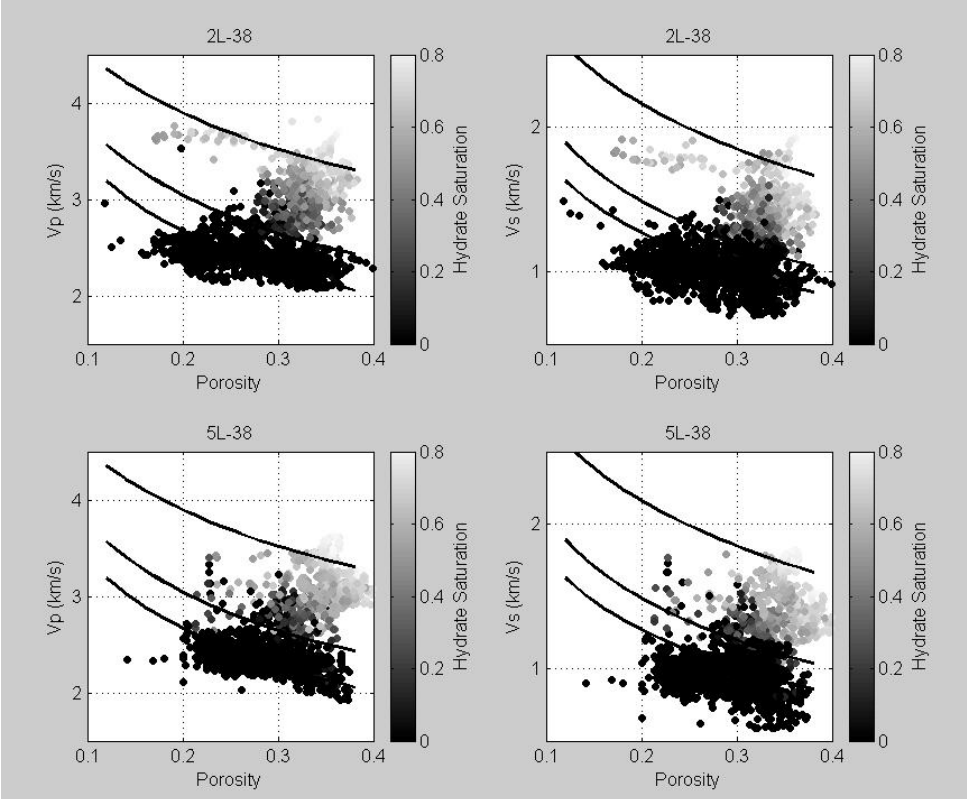

Figure 6.2. Mallik wells 2L-38 (top) and 5L-38 (bottom). *P*- (left) and *S*-wave velocity (right) versus the porosity of the mineral frame (without hydrate) color-coded by hydrate saturation. The model curves are (from top to bottom) for 0.8, 0.4, and zero hydrate saturation in the clean host sand. The data points falling below the zero hydrate saturation curves are from intervals with clay.

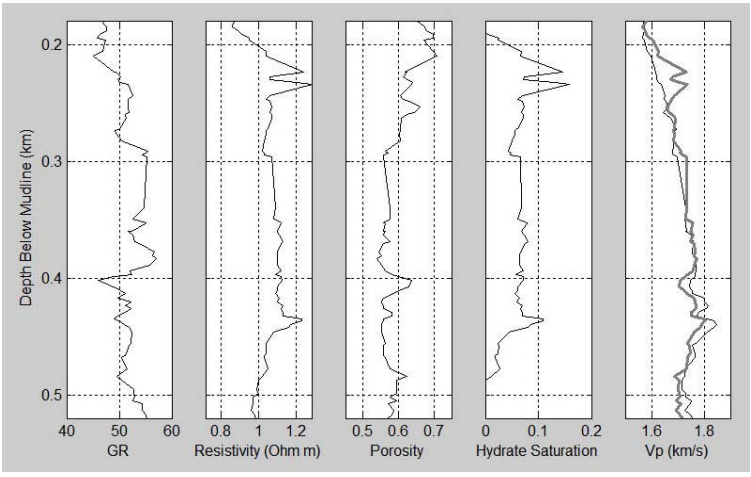

Figure 6.3. Well 995 at the Outer Blake Ridge depth curves. From left to right – GR; resistivity; porosity of the mineral frame without gas hydrate; hydrate saturation; and *P*-wave velocity measured (black) and reproduced by the soft-sand model (red).

The final field example is from yet another depositional environment which is in Nankai Trough offshore Japan where gas hydrate occurs in the sandy parts of the interval (low GR) and is characterized by elevated *P*- and *S*-wave velocity and strong positive reflection. The velocity data are plotted versus the porosity of the mineral frame (without hydrate) and color-coded by hydrate saturation in Figure 6.4. The curves superimposed upon the data are from the soft-sand model used in the two previous examples. In this specific case we assumed that the sand with hydrate contains 10% clay with the rest of the mineral being quartz. Once again, the model curves provide a reasonable match to the data.

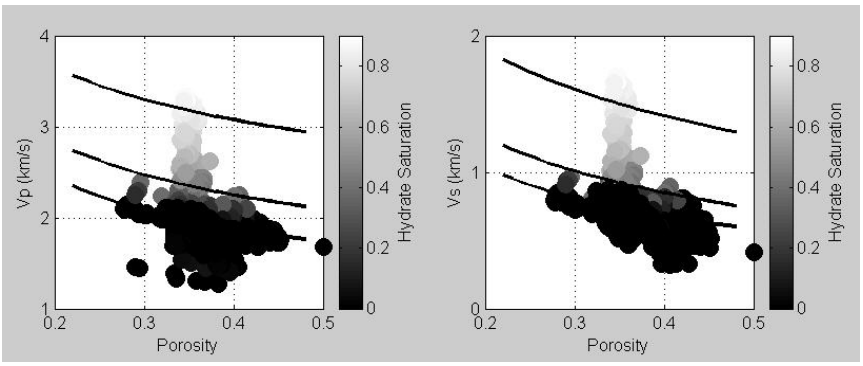

Figure 6.4. Velocity data from two Nankai Trough wells. *P*- (left) and *S*-wave velocity (right) versus porosity of the mineral frame (without hydrate) color-coded by hydrate saturation. The soft-sand model curves are (from top to bottom) for 0.8, 0.4, and zero hydrate saturation in clean sand with 10% clay. The data points falling below the zero hydrate saturation curves are from intervals with clay.

7. USING ROCK PHYSICS IN PREDICTIVE MODE – MATLAB APPLETS

The examples presented in the previous section indicate that the soft-sand model (the modified lower Hashin-Shtrikman bound or model "b"), with gas hydrate accounted for as part of the solid frame, is likely to be the most appropriate model for predicting the elastic properties in methane hydrate reservoirs discovered so far. Of course, well data from each new discovery have to be analyzed to further confirm (or refute) this statement and find the most appropriate rock physics model.

Now that we have established a rock physics model and validated it with real data, the next step is to use it in a predictive mode to assess the seismic signature of methane hydrate away from well control in "what-if" mode. We have conducted this type of

synthetic modeling and collected the results of this modeling to develop a catalogue of the seismic signatures of methane hydrate as they vary versus hydrate volume, properties and conditions of the host sediment, and the properties of the background, e.g., shale, sand, or calcareous marine sediment without hydrate. In addition, this modeling allows us to construct a pseudo-earth model (a pseudo-well), vary its properties and conditions to try to match the observed seismic traces and attributes away from well control, and, by so doing, quantitatively estimate what rock properties may stand behind the recorded seismic response. Note that this approach to hydrate reservoir characterization results in non-unique solutions, because the elastic reflection depends on the contrast of the elastic properties at an interface rather than on their absolute values.

Various combinations of rock properties and conditions in the reservoir and background may produce the same reflection. This non-uniqueness can only be alleviated by the use of geologic and stratigraphic constraints on porosity, mineralogy, and reservoir geometry.

An example of reflectivity modeling at a methane hydrate reservoir is given in Figure 7.1. The main panel is an acoustic impedance $I_p = \rho_b V_p$ versus Poisson's ratio $\nu = 0.5(V_p^2/V_s^2 - 2)/(V_p^2/V_s^2 - 1)$ cross-plot where the elastic properties of shale, sand with varying hydrate saturation, and gas sand are mapped according to the soft-sand model. The porosity in the shale varies between 0.3 and 0.7 while the clay content is between 0.5 and 1.0. The porosity in the sand is between 0.3 and 0.4 with clay content fixed at 0.1. The methane hydrate saturation varies between zero (wet sand) and 0.8.

To model an AVO curve we select two consecutive points in the I_p-ν plane which represent the overburden and reservoir, respectively. Next, we select the net-to-gross value which is measured in the units of a quarter-wavelength. If the net-to-gross value is a fraction of the quarter-wavelength (a half in the example in Figure 7.1), we calculate the elastic properties of the lower elastic half-space by averaging those of the reservoir and the overburden according to the Backus (1962) scheme. Finally, the amplitude versus angle is calculated using the Zoeppritz (1919) equations. The resulting amplitude-versus-angle curve is plotted in a bottom-left panel and its intercept and gradient in the bottom-right panel.

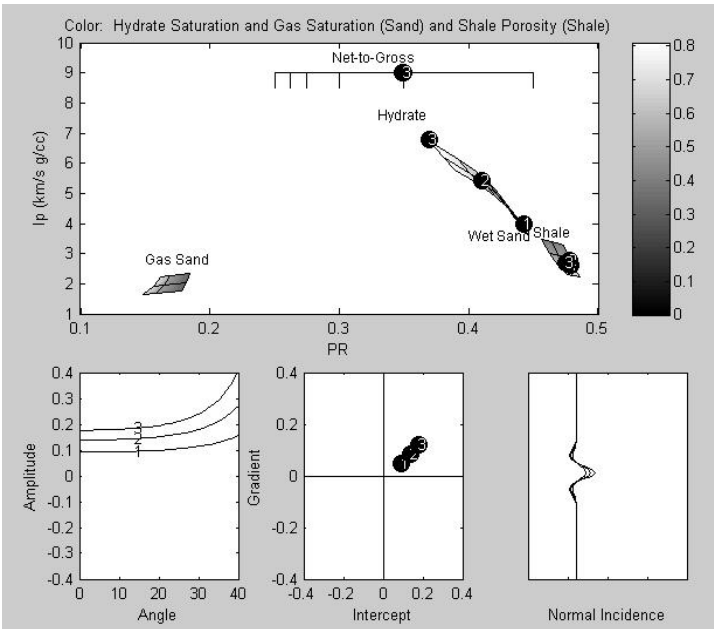

Figure 7.1. Reflectivity modeling at an interface with a methane hydrate reservoir. From overburden shale to wet sand (1); sand with small hydrate saturation (2); and sand with large hydrate saturation (3). The net-to-gross value is 0.5. Color coding is explained in the panel title.

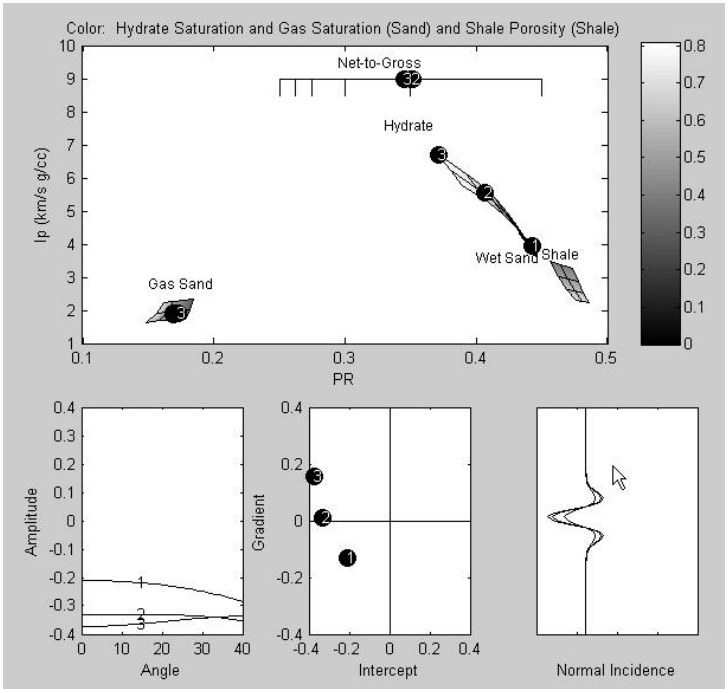

Figure 7.2. Same as in Figure 7.1 but modeling reflections between sand with hydrate (overburden) and gas sand. From wet sand to gas sand (1); from sand with small hydrate saturation to gas sand (2); and from sand with large hydrate saturation to gas sand (3).

The example in Figure 7.1 shows how the AVO curve changes as the properties of the overburden shale remain fixed while the hydrate saturation in the sand below increases from zero to about 0.8. The example in Figure 7.2 explores reflections between sand with progressively increasing amounts of hydrate and gas sand whose properties remain fixed. The net-to-gross ratio, i.e., the thickness of the layer beneath the reflecting interface, is fixed at 1/8 of the wavelength. These results indicate that the amount of hydrate has the primary influence on the reflections while that of gas saturation is negligible.

A relevant rock physics model can also be used to explore the sensitivity of the reflection to the properties of the overburden and reservoir. An example in Figure 7.3 shows the normal reflection amplitude between shale of continuously varying porosity and clay content and a hydrate sand with varying porosity and hydrate saturation.

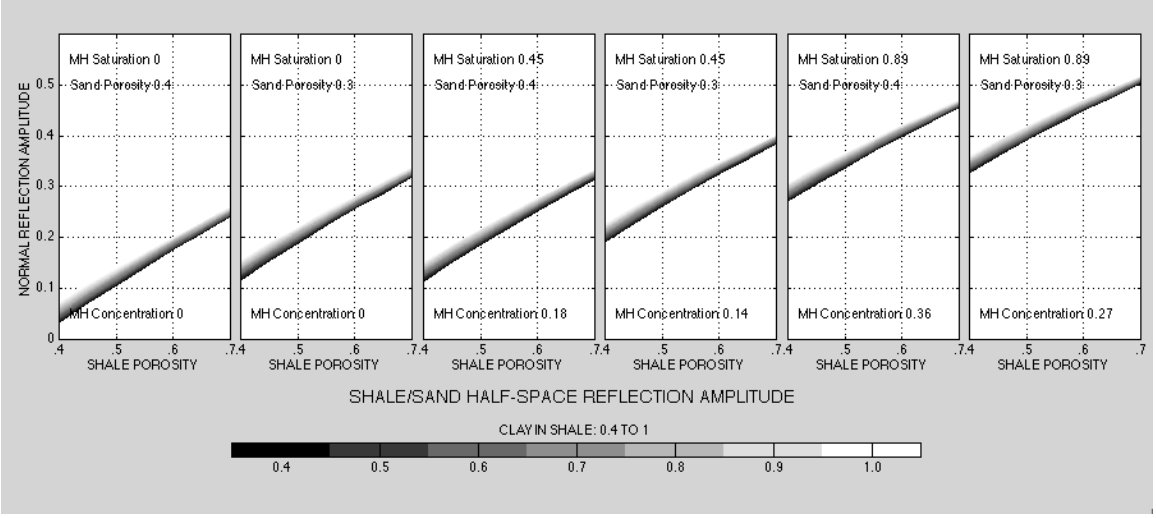

Figure 7.3. Normal reflection amplitude at the interface between shale and sand (both are treated as infinite half-spaces). The soft-sand model is used for both shale and sand. The horizontal axis in all frames is the total porosity of the shale. The color-code is the clay content in the shale which varies between 0.4 and 1.0. In the first and second frames, the hydrate saturation in the sand is zero while the porosity of the sand is 0.4 (left) and 0.3 (right). In the next two frames, the hydrate saturation is 0.45 with all other parameters being the same as in the first two frames. In the final two frames, the hydrate saturation is 0.9. The hydrate concentration which is the product of the sand porosity and hydrate saturation is also displayed in the frames.

We observe that the reflection is strongly affected by the porosity (degree of

consolidation) of the shale overburden while the clay content in the shale has much less influence. A strong positive reflection can occur between very unconsolidated shale and wet sand without hydrate. The magnitude of this seismic event may be comparable to that between more consolidated shale and sand with about 50% hydrate saturation. The porosity of the sand is important as well. Only at very high hydrate saturation is the reflection amplitude strong enough to be markedly different from that between shale and wet sand no matter what the porosity of the strata.

Arguably, the quantity of interest in hydrate exploration is not the hydrate saturation of the pore space but rather the hydrate concentration in a unit volume of sediment which is the product of the total porosity of the host sediment and hydrate saturation in the pore space. Figure 7.3 indicates that, due to variation in the sand porosity, the reflection from a reservoir with hydrate concentration 0.27 can be stronger than that from a reservoir with hydrate concentration 0.36. This fact emphasizes the importance of using geologically and depositionally plausible parameters, such as porosity of sand and shale, in forward modeling. It also highlights the non-uniqueness of quantitative seismic interpretation. Specifically, a stronger amplitude may not mean more hydrate; it may result from a lower-porosity sand or higher-porosity shale.

An example of combining the soft-sand methane hydrate model with a layered earth model and synthetic seismic trace generator is shown in Figure 7.4. This is an interactive process where the porosity of the background shale and its clay content are selected first.

Selected next is the profile of hydrate and free gas saturation. Based on this background data and assuming fixed porosity and clay content in the sand, the model is used to produce the velocity and density depth curves which, in turn, serve as input into a synthetic seismic generator.

The example in Figure 7.4 indicates that the dominant seismic event is a large trough due to the gas sand. The peak at the top of the hydrate layer can be easily misinterpreted as a side-lobe of the main trough. The lack of a strong AVO effect at this peak, unlike in the bottom side-lobe, is a subtle indicator of gas hydrate in this case.

The example in Figure 7.5 shows reflections due to hydrate without free gas underneath. We observe a peak-trough sequence without a significant AVO effect which

is characteristic of sand filled with hydrate and water, without free gas.

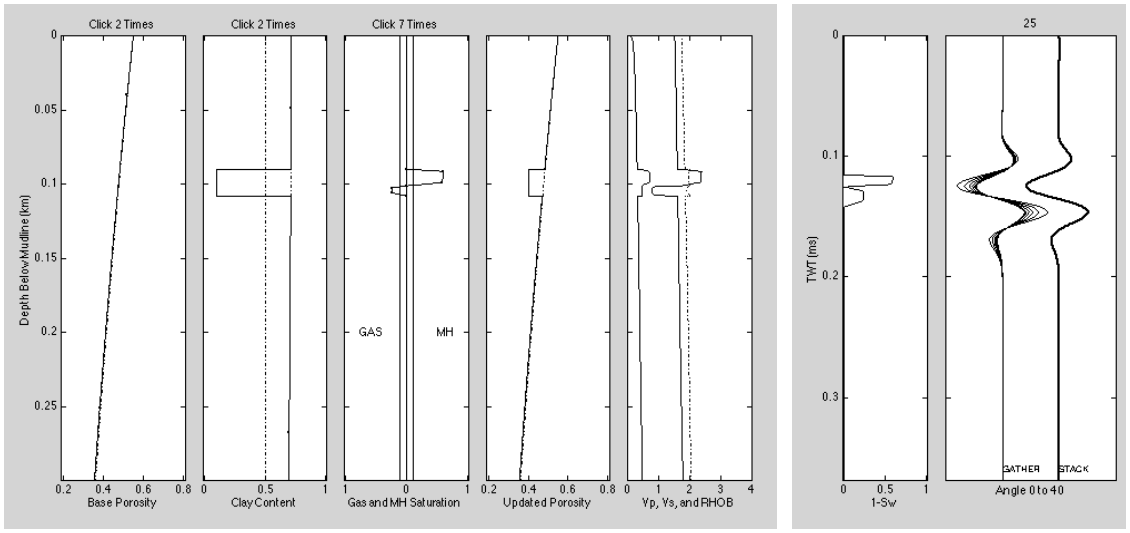

Figure 7.4. Synthetic traces, gather and full stack (right), generated on the earth model constructed in the left-hand frames. The porosity of the sand is fixed at 0.4 while its clay content is 0.1. In the first four frames, the dotted curves are for default parameters while the solid curves are for interactively selected parameters. In the fifth frame, the bulk density is shown as dotted curve while the P- and S-wave velocity curves are solid. A ray-tracer with a Ricker 25 Hz wavelet is used to generate synthetic seismic traces. In this example, the hydrate sand with high hydrate saturation is immediately followed by sand with very small gas saturation.

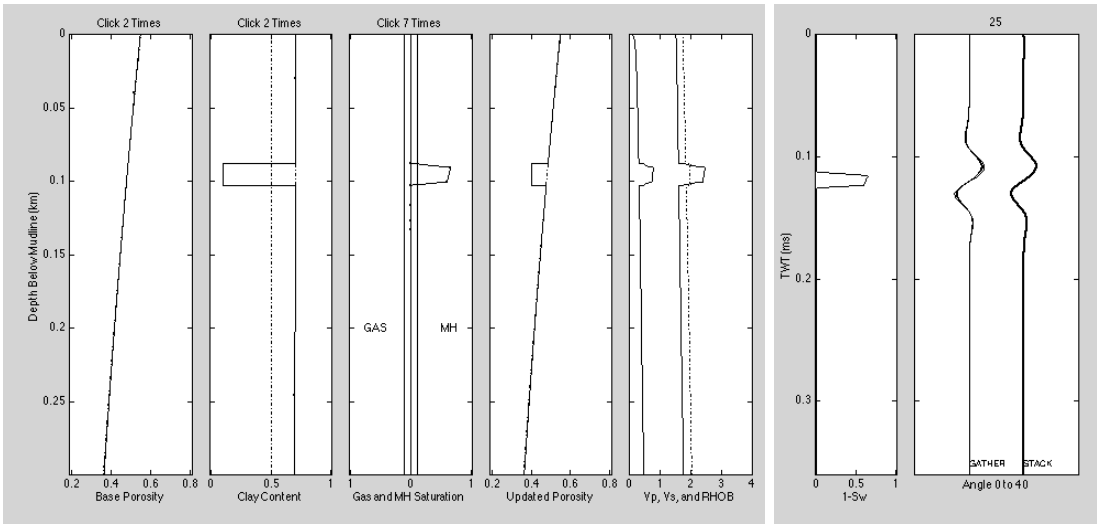

Figure 7.5. Similar to Figure 7.4 but without free gas sand underneath the hydrate sand.

Finally, in Figure 7.6 we show reflections of hydrate sand with wedge-shaped hydrate

saturation profile and free-gas sand separated from the hydrate by a shale layer. The dominant feature in the seismic profile is a trough at the top of free gas with a strong AVO effect. The reflection from the hydrate is comparatively weak, with the main feature being a trough at the base of the hydrate.

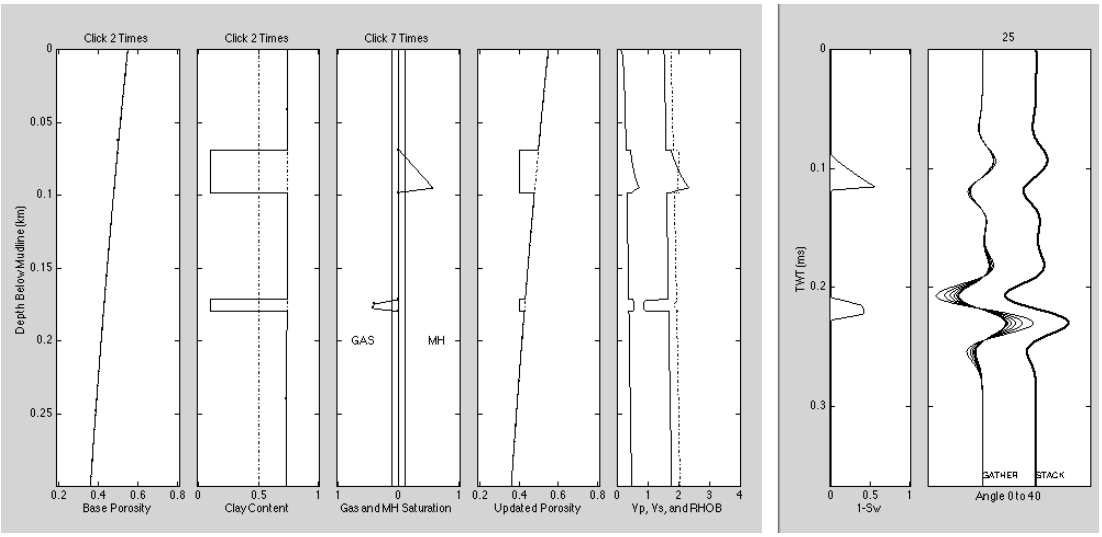

Figure 7.6. Similar to Figure 7.4 but with wedge-shaped hydrate saturation profile and gas sand separated from the hydrate sand.

These examples not only elucidate the possible ambiguity of the seismic reflections of a hydrate reservoir but also show how to use rock physics to explore variants of the seismic response and, by so doing, quantitatively interpret field observations and constrain a spectrum of possibilities.

8. EXPLAINING REAL TRACES

Consider a full-stack seismic section from the Hydrate Ridge in Figure 2.1 (left). Our goal is to quantify the events that stand out of the background in terms of methane hydrate content. The first step is to examine the well data at the site to establish a rock physics transform. The data from the first well (Figure 8.1, top) drilled through the strong seismic events (arguably, a BSR) do not exhibit well-pronounced signs of methane hydrate. The GR curve points to two sandy intervals between 1.06 and 1.09 km depth. The resistivity in this sand exceeds the background which is a possible indication of hydrate (and/or gas). However, it may also be a result of the porosity in the sand being

smaller than in the surrounding shale. The sonic MWD curve fails to exhibit any significant hydrate-triggered velocity increase in the sand. However, unlike V_p, V_s has a discernable peak concurrent with the resistivity peak.

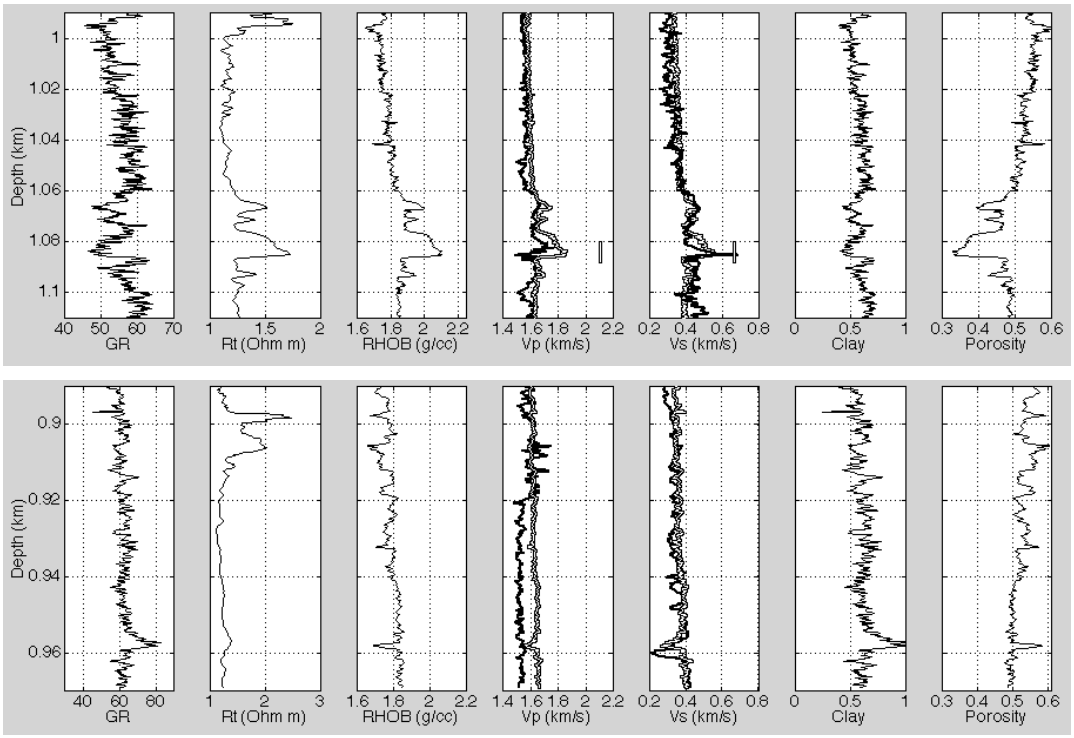

Figure 8.1. Two wells from the Hydrate Ridge (data courtesy Nathan Bangs of UT Austin). The clay curves are calculated by linearly scaling GR. The porosity is calculated form density by assuming that the mineral density is 2.65 g/cc and that of water is 1.00 g/cc. The bold black curves in the velocity frames are from MWD data while the hollow black curves are from the soft-sand model assuming zero hydrate saturation. The vertical hollow black bars (display on the top) are from the same model but assuming 0.3 hydrate saturation.

To mimic the velocity data, we use the soft-sand model and apply it to the entire interval where the porosity is calculated from the bulk density as $\phi = (2.65 - \rho_b)/1.65$ and the clay content was estimated by linearly scaling the GR curve. The model velocity curves produced under the assumption that there is no hydrate in the well lie fairly close to the V_p and V_s data except for the lower sand interval where the model overestimates V_p but underestimates V_s. Let us assume that the V_s data are more trustworthy than V_p. Then the peak in V_s can be explained by the presence of methane hydrate. Indeed, the modeled velocity (vertical bars in the velocity frames) with hydrate saturation 0.3

matches the V_s data. The main result of this exercise is that the soft-sand model, once again, is a good candidate for translating porosity, mineralogy, and hydrate saturation into velocity and density.

Applying this model to the second well (where hydrate is absent) confirms this conclusion for the *S*-wave curve and makes us doubt the validity of the sonic curve below 920 m (Figure 8.1, bottom).

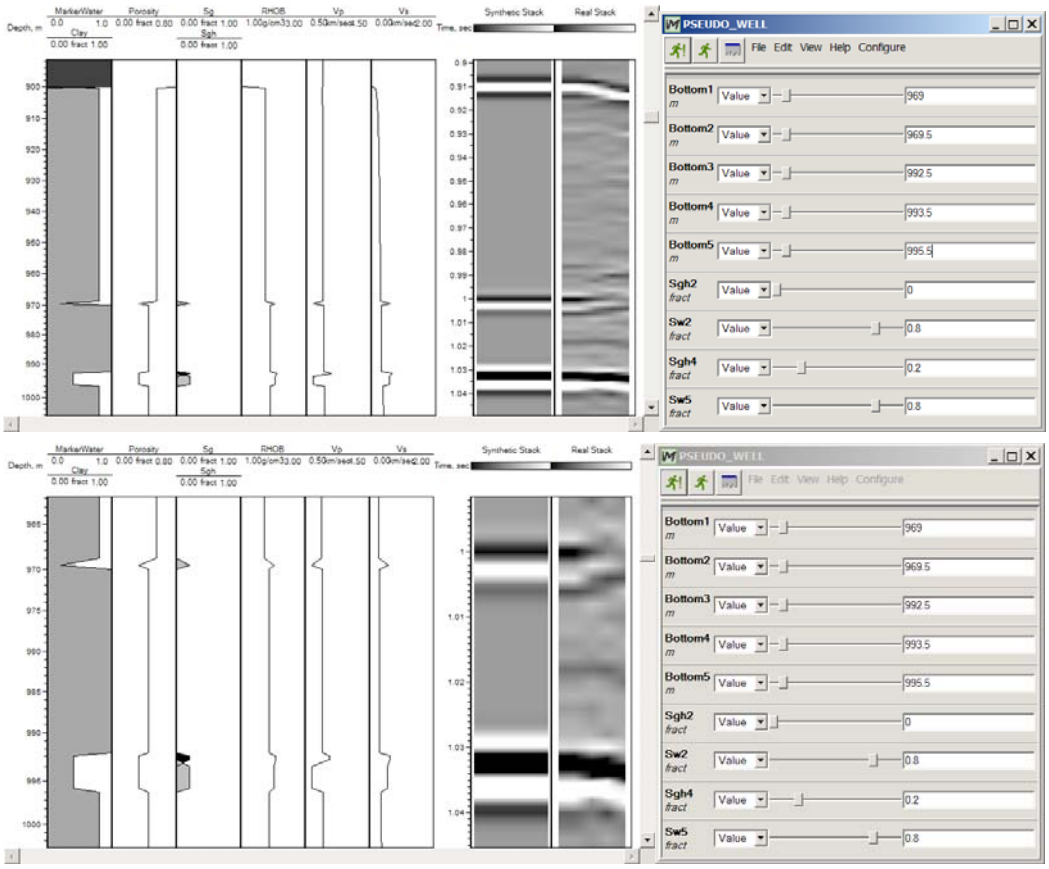

Figure 8.2. The Hydrate Ridge full-stack section with a synthetic stack to the left. Top – sections with the sea-bottom reflection. Bottom – zoom on the main events. White is peak while black is trough. The clay content, porosity, and hydrate and free gas saturation curves in the pseudo-well are displayed on the left. The resulting density and velocity profiles are next, followed by the synthetic and real stacks. The interactive panel with the depths of the layer bottoms and water and hydrate saturations in the layers is shown on the right. The upper sand layer contains free gas while the lower layer has hydrate with free gas underneath. In the third-from-left track, black is for hydrate while gray is for gas. The interactive panels on the left specify the geometry of the layers as well as water saturation in the free-gas layers ("Sw2" and "Sw5") and hydrate saturation in sand layers ("Sgh2" and "Sgh4").

Next, we construct a 1D model of earth that includes the sea-water column (Figure 8.2). The layers in this model are shale and sand with user-selected porosity and clay content. A ray-tracer with a Ricker (120 Hz) wavelet is used to produce the full stack of a synthetic seismic gather.

The first task is to calibrate the amplitude of synthetic stack to the real seismic event at the sea bottom. Once this is achieved, various hydrate and free gas saturations can be assigned to the two sand layers in the model to match the reflections underneath. A satisfactory match can be achieved by assuming that there is residual gas in the upper sand layer while hydrate saturation is 0.2 in the second layer with a residual gas layer underneath (Figure 8.2).

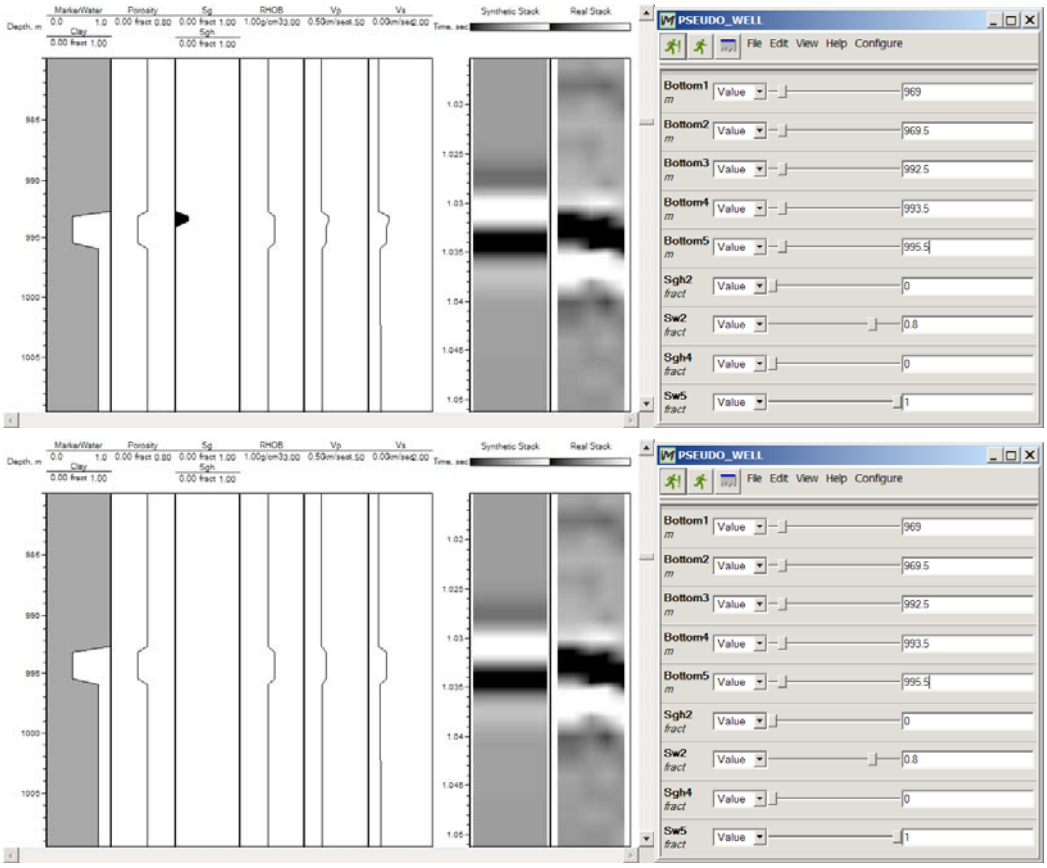

Figure 8.3. Same as Figure 8.2 but without free gas in the pseudowell, and with (top) and without (bottom) hydrate present.

The next question is whether this match is unique or can be achieved with different earth model parameters. Figure 8.3 indicates that the observed seismic feature has to be

associated with free gas. Otherwise, the observed peak-trough-peak triplet cannot be matched whether or not hydrate is present.

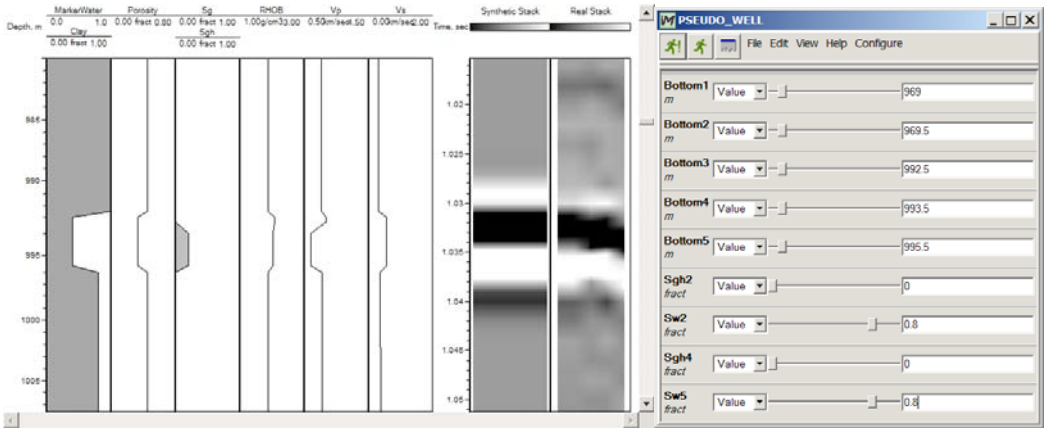

Figure 8.4. Same as Figure 8.2 but without hydrate and with free gas.

Let us next keep the free-gas layer and remove hydrate. Figure 8.4 indicates that we can still reach a synthetic-to-real match even if the hydrate is absent in the sand. This example emphasizes the non-uniqueness of seismic interpretation even if an appropriate rock physics model is used.

Needless to say, an interpretation of standard impedance inversion, although providing a correct impedance section, will also be ambiguous in terms of rock properties and conditions. The physical foundation of the observed ambiguity is that small amounts of hydrate do not affect the impedance in the sand to the point that the presence of a methane hydrate reservoir can be established without doubt.

This example also points to the importance of geological reasoning in such interpretation. If the observed BSR can be explained solely by the presence of free gas, one has to ask what is the seal that sequesters this gas and why it has a classical BSR shape. An answer could be that the only possibility is sealing by methane hydrate that occupies the pores and essentially eliminates the relative gas permeability. This argument, in favor of the presence of hydrate, needs to be further supported by geochemical proof that the observed feature falls within the hydrate stability window with hydrostatic pressure and temperature gradient as input.

In contrast to the Hydrate Ridge case, the next example shows that large hydrate

quantities can be detected and interpreted with reasonable certainty (Figure 8.5). In this case, the calibration of the synthetic seismic amplitude to real data is accomplished on the free-gas event that is separate from the BSR and lies underneath it. It is apparent from the modeling results that only a significant amount of hydrate can produce the bright event evident in the real data. In this case, the presence of large amounts of hydrate has been also directly confirmed by drilling.

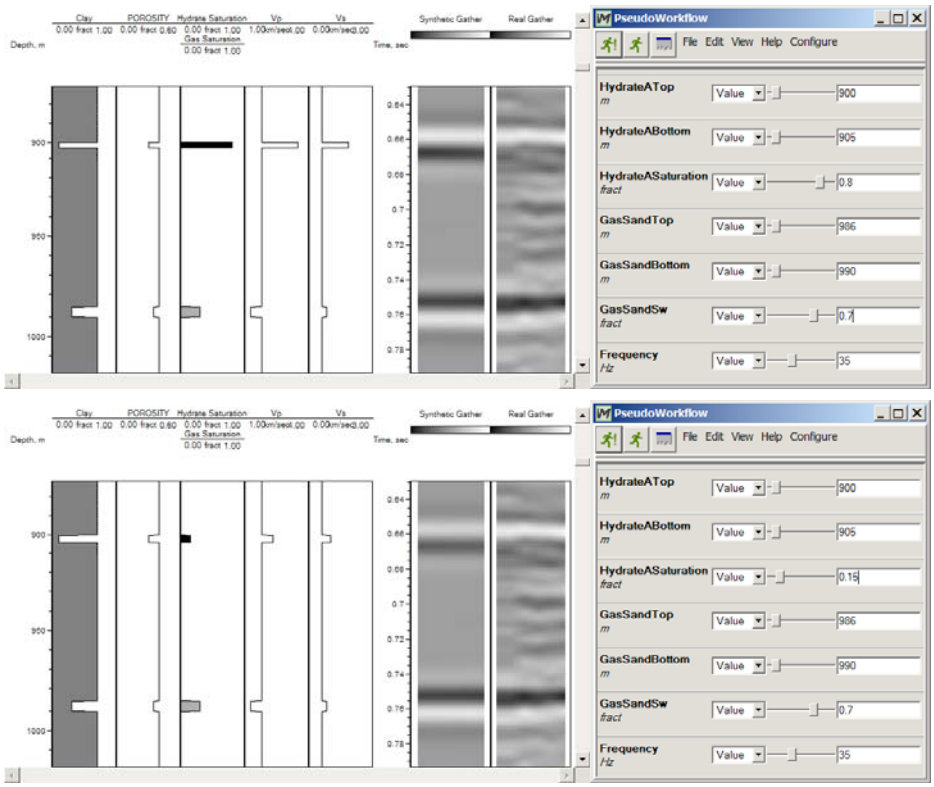

Figure 8.5. Real (right) and synthetic (left) gathers at an offshore BSR location. The display is similar to Figure 8.3. Top – large hydrate saturation. Bottom – smaller hydrate saturation.

Figure 8.6 displays variants of synthetic seismic modeling with the absence of hydrate (top) and absence of gas (bottom). We learn that (a) wet sand can produce an event qualitatively similar to the observed BSR but much weaker and (b) the lower event can only be attributed to the presence of free gas.

Once again, reasonable confidence in this interpretation needs to be supported by geology and geochemistry. An additional type of prospecting, such as CSEM, may help to further de-risk a prospect, based on the fact that gas hydrate is a dielectric and thus has

high resistivity.

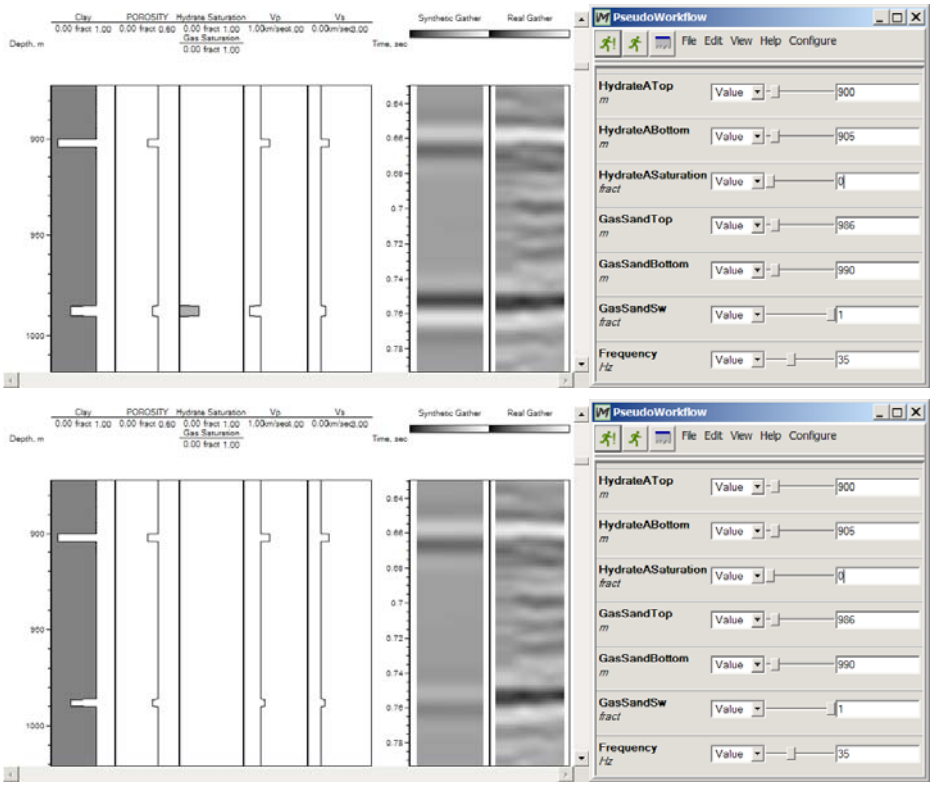

Figure 8.6. Same as Figure 8.5 but without hydrate in the pseudowell, and with (top) and without (bottom) free gas.

9. CATALOGUE OF SEISMIC REFLECTIONS

Using the forward-modeling principle advocated here, we developed a catalogue of some possible seismic reflections that could be expected from methane hydrate reservoirs. An example is shown in Figure 9.1, where the sediment properties are selected similar to those at Hydrate Ridge. This example illustrates that not only the hydrate and free gas amounts affect the reflection but also the porosity of the sand and background shale.

To create the synthetic seismic output displayed in a catalogue, we first specify the conditions in the subsurface, which include the clay content, porosity, and hydrate and free gas saturations. Next, rock physics equations are used to translate these conditions into the elastic-wave velocity and bulk density. Finally, the output synthetic seismic traces are computed for this earth model.

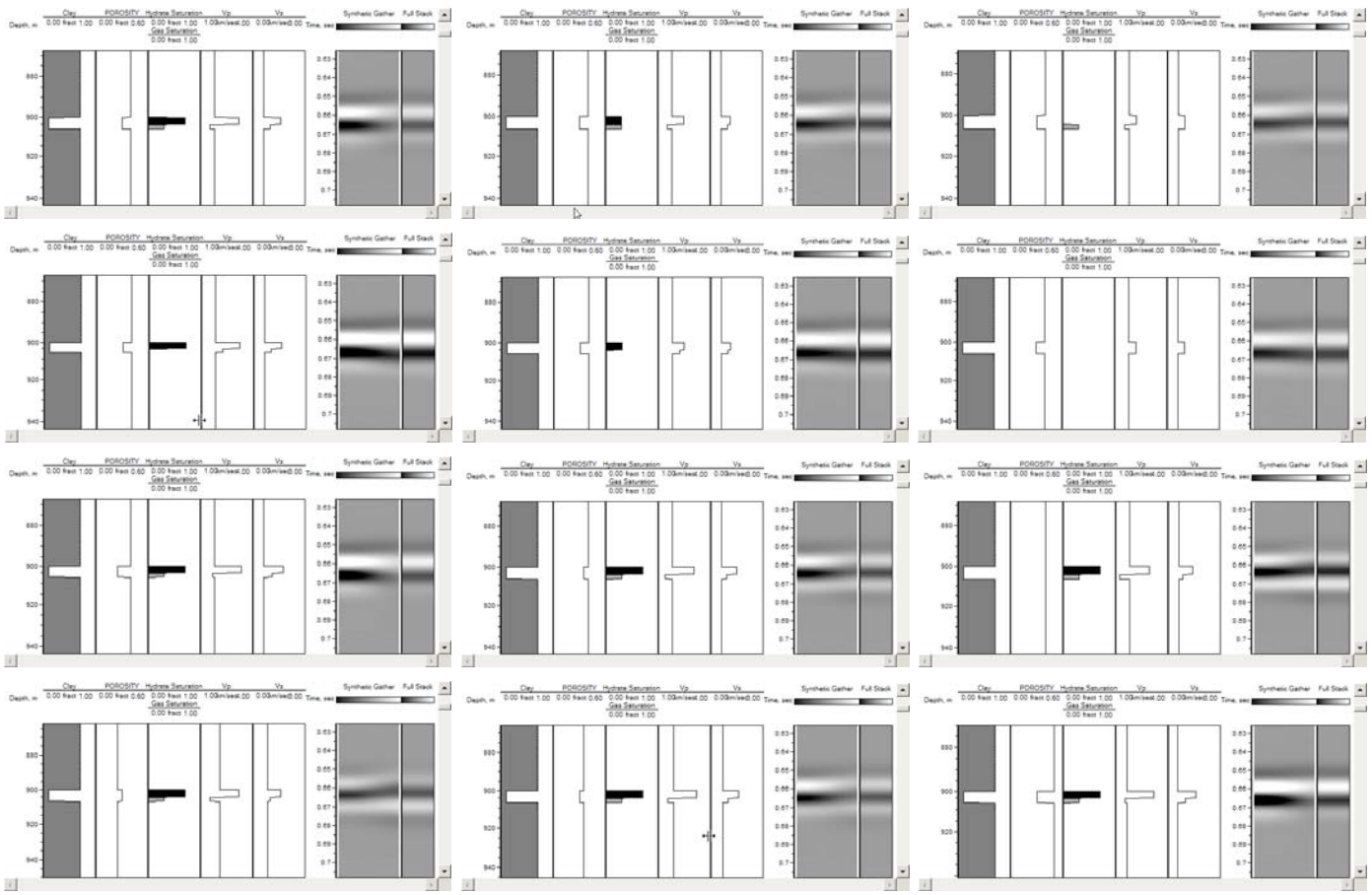

Figure 9.1. A rock-physics-based catalogue of the seismic reflections (full stacks and gathers) of disjoined gas hydrate and free gas layers. The display is similar to Figures 8.2 to 8.6. Top row: hydrate with free gas directly underneath. The amount of hydrate is reduced from left to right. Second row: hydrate without free gas. The amount of hydrate is reduced from left to right. Third row: hydrate with free gas underneath. The porosity of the sand layer increases from left to right. Bottom row: hydrate with free gas underneath. The porosity of shale increases from left to right.

CONCLUSION

We developed rock physics equations that link the properties and conditions of a natural methane hydrate reservoir to its elastic properties. These equations can be used to create synthetic seismograms of the reservoir's seismic response. This technique, combined with complementary geologic and geochemical considerations, can help quantify hydrate reservoir quality and hydrate saturation from seismic data. Catalogues of synthetic traces may serve as a field guide to hydrate quantification. They also allow the interpreter to interactively assess the ambiguity of such quantification.

The use of a first-principle-based model is critical for hydrate characterization because only within a physics-based framework can one consistently perturb reservoir properties and conditions to estimate the elastic response with the ultimate goal of characterizing the reservoir from field elastic data. Of course, this approach relies on the assumption that the same model is appropriate at all instances -- which should not be taken for granted (see Appendix III for a different model where pure hydrate lenses are embedded into a shale background).

Intrinsic and scattering attenuation (Appendix I) due to the presence of massive layers of hydrate may affect the seismic amplitude and must therefore be taken into account during modeling and interpretation of seismic data. It can also serve as an indicator of gas hydrate saturation in a reservoir. Reservoir geometry and thickness affect the seismic amplitude. Therefore, rock physics relations have to be used with caution to become applicable to seismic reservoir characterization if seismically-derived acoustic and elastic impedances are used (Appendix II).

The forward-modeling approach reported here results in non-unique solutions, because different combinations of rock properties may produce the same reflections. To constrain the spectrum of answers, the earth model used in the modeling has to be geologically-plausible, including ranges of porosity and clay content in the layers which are permissible within the hydrate stability window defined by the pore pressure and temperature.

Finally, it is crucial to validate the possibility of methane hydrate or free gas

occurrence by applying geologic constraints to the solutions based on the forward-modeling principle.

ACKNOWLEDGEMENTS

Huyen Bui of Schlumberger and Nathan Bangs of UT Austin helped obtain and display the Hydrate Ridge seismic and well data. iMOSS was provided by Rock Solid Images.

REFERENCES

Avseth, P., Dvorkin, J., Mavko, G., and Rykkje, J., 2000, Rock physics diagnostic of North Sea sands: Link between microstructure and seismic properties, GRL, 27, 2761-2764.

Backus, G.F., 1962, Long-wave elastic anisotropy produced by horizontal layering, JGR, 67, 4427-4441.

Bangs, N. L., D. S. Sawyer and X. Golovchenko, 1993, Free gas at the base of the gas hydrate zone in the vicinity of the Chile triple junction, Geology, 21, 905-908.

Batzle, M., and Wang, Z., 1992, Seismic properties of pore fluids, Geophysics, 57, 1396-1408.

Cordon, I., Dvorkin, J., and Mavko, G., 2006, Seismic reflections of gas hydrate from perturbational forward modeling, Geophysics, 71, F165-F171.

Dai, J., Xu, H., Shyder, F., and Dutta, N.., 2004, Detection and estimation of gas hydrates using rock physics and seismic inversion: Examples from the northern deepwater Gulf of Mexico, The Leading Edge, 23, 60-66.

Dickens, G. D., C. K. Paull, and P. Wallace, 1997, Direct Measurement of in situ methane quantities in a large gas hydrate reservoir, Nature, 385, 426-428.

Dvorkin, J., Nur, A., and Yin, H., 1994, Effective Properties of Cemented Granular Materials, Mechanics of Materials, 18, 351-366.

Dvorkin, J., and Nur, A., 1996, Elasticity of high-porosity sandstones: Theory for two north sea datasets, Geophysics, 61, 1363-1370.

Dvorkin, J., 1996, Large Strains in Cemented Granular Aggregates: Elastic-Plastic

Cement, Mechanics of Materials, 23, 29-44.

Dvorkin, J., and Nur, A., 1998, Time-Average Equation Revisited, Geophysics, 63, 460-464.

Dvorkin, J., Prasad, M., Sakai, A., and Lavoie, D., 1999, Elasticity of marine sediments, GRL, 26, 1781-1784.

Dvorkin, J., Nur, A., Uden, R., and Taner, T., 2003, Rock physics of gas hydrate reservoir, The Leading Edge, 22, 842-847.

Dvorkin, J., and Uden, R., 2004, Seismic wave attenuation in a methane hydrate reservoir, The Leading Edge, 23, 730-734.

Ecker, C., Dvorkin, J., and Nur, A., 2000, Estimating the amount of gas hydrate and free gas from marine seismic data, Geophysics, 65, 565-573.

Gassmann, F., 1951, Elasticity of porous media: Uber die elastizitat poroser medien: Vierteljahrsschrift der Naturforschenden Gesselschaft, 96, 1-23.

Guerin, G., Goldberg, D., and Meltzer, A., 1999, Characterization of in-situ elastic properties of gas-hydrate-bearing sediments on the Blake Ridge, JGR, 104, 17781-17796.

Guerin, G., and Goldberg, D., 2002, Sonic waveform attenuation in gas-hydrate-bearing sediments from the Mallik 2L-38 research well, Mackenzie Delta, Canada, JGR, 107, 1029-1085.

Hashin, Z., and Shtrikman, S., 1963, A variational approach to the elastic behavior of multiphase materials, Journal of Mechanics and Physics of Solids, 11, 127-140.

Helgerud, M., Dvorkin, J., Nur, A., Sakai, A., and Collett, T., 1999, Elastic-wave velocity in marine sediments with gas hydrates: Effective medium modeling, GRL, 26, 2021-2024.

Helgerud, M., 2001, Wave speeds in gas hydrate and sediments containing gas hydrate: A laboratory and modeling study, Ph.D. thesis, Stanford University.

Hill, R., 1952, The elastic behavior of crystalline aggregate, Proc. Physical Soc., London, A65, 349-354.

Holbrook, W. S., H. Hoskins, W. T. Wood, R. A. Stephen, D. Lizarralde, 1996, Methane Hydrate and Free Gas on the Blake Ridge from Vertical Seismic Profiling, Science,

273, 1840-1843.

Hudson, J.A., 1990, Overall elastic properties of isotropic materials with arbitrary distribution of circular cracks, Geophys. J. Int., 102, 465-469.

Hyndman, R. D. and G. D. Spence, 1992, A Seismic Study of Methane Hydrate Marine Bottom Simulating Reflectors, JGR, V97, 6683-6698.

Lee, M.W., Hutchinson, D.R., Collett, T.S., and Dillon, W.P., 1996, Seismic velocities for hydrate-bearing sediments using weighted equation, JGR, 101, 20,347-20,358.

Lee, M.W., 2002, Biot-Gassmann theory for velocities of gas hydrate-bearing sediments, Geophysics, 67, 1711-1719.

Mavko, G., T. Mukerji, J. Dvorkin, 1998, The Rock Physics Handbook: Tools for Seismic Analysis in Porous Media, Cambridge University Press, New York, 329.

Minshull, T. A., Singh, S.C., and Westbrook, G.K., 1994, Seismic velocity structure at a gas hydrate reflector, offshore western Colombia, from full waveform inversion, JGR, 99, 4715-4734.

Miller, J. J., M. W. Lee and R. von Huene, 1991, An analysis of a Seismic Reflection from the base of a gas hydrate zone, offshore Peru, AAPG Bull., 75, 910-924.

Mindlin, R. D., 1949, Compliance of elastic bodies in contact, Trans. SDME, 71, A-259.

Nur, A., Mavko, G., Dvorkin, J., and Galmudi, D., 1998, Critical Porosity: A Key to Relating Physical Properties to Porosity in Rocks, The Leading Edge, 17, 357-362.

O'Doherty, R.F., and Anstey, N.A., 1971, Reflections on amplitudes, Geophysical Prospecting, 19, 430-458.

Koesoemadinata, A.P, and McMechan, G.A., 2001, Empirical estimation of viscoelastic seismic parameters from petrophysical properties of sandstone, Geophysics, 66, 1457-1470.

Pearson, C., J. Murphy and R. Hermes, 1986, Acoustic and Resistivity Measurements on Rock Samples Containing Tetrahydrofuran Hydrates: Laboratory Analogues to Natural Gas Hydrate Deposits, JGR, 91, 14132-14138.

Paull, C.K., Matsumoto, R., Wallace, P.J., et al., 1996. Proc. ODP, Init. Repts., 164: College Station, TX (Ocean Drilling Program).

Pratt, R.G., Bauer, K., and Weber, M., 2003, Cross-hole waveform tomography velocity

and attenuation images of arctic gas hydrates, Expanded Abstract, SEG International Exposition and Seventy-Third Annual Meeting.

Prasad, M., and Dvorkin, J., 2001, Velocity to porosity transform in marine sediments, Petrophysics, 42, 5, 429-437.

Pride, S.R., Harris, J.M., Johnson, D.L., Mateeva, A., Nihei, K.T., Nowack, R.L., Rector, J.W., Spetzler, H., Wu, R., Yamamoto, T., Berryman, J.G., and Fehler, M., 2003, Permeability dependence of seismic amplitudes, TLE, 22, 518-525.

Reuss, A., 1929, Berechnung der Fliessgrenzev von Mischkristallen auf Grund der Plastizitätsbedingung für Einkristalle, Zeitschrift für Angewandte Mathematik und Mechanik, 9, 49-58.

Sakai, A., 1999, Velocity analysis of vertical seismic profiling (VSP) survey at Japex/JNOC/GSC Mallik 2L-38 gas hydrate research well, and related problems for estimating gas hydrate concentration, GSC Bulletin, 544, 323-340.

Scholl, D. W. and P. E. Hart, 1993, Velocity and Amplitude Structures on Seismic-Reflection Profiles–Possible Massive Gas-Hydrate Deposits and Underlying Gas 2005.

Schlumberger, 1991, Log Interpretation Principles/Applications, Reference Book.

Wood, W. T., P. L. Stoffa and T. H. Shipley, 1994, Quantitative detection of methane hydrate through high-resolution seismic velocity analysis, JGR, 99, 9681-9695.

Wyllie, M.R.J., Gregory, A.R., and Gardner, L.W., 1956, Elastic wave velocities in heterogeneous and porous media, Geophysics, 21, 41-70.

Wood, A.W., 1955, A textbook of sound, The MacMillan Co., NY, 360.

Wood, W.T., Holbrook, W.S., and Hoskins, H., 2000, In situ measurements of P-wave attenuation in the methane hydrate–and gas-bearing sediments of the Blake Ridge, in Proceedings of the ODP, Scientific Results, 164, Paull, C.K., Matsumoto, R., Wallace, P.J., and Dillon, W.P. (Eds.), 265-271.

Wyllie, M.R.J., Gregory, A.R., and Gardner, L.W., 1956, Elastic wave velocities in heterogeneous and porous media, Geophysics, 21, 41-70.

Zoeppritz, K., 1919, Erdbebenwellen VIIIB, On the reflection and propagation of seismic waves. Goettinger Nachrichten, I, 66-84.

APPENDIX I. ATTENUATION IN METHANE HYDRATE

Elastic-wave data collected in sediments with methane hydrate around the world point to significant velocity increase due to the presence of the hydrate in the pores. This effect can be easily understood if we recall that gas hydrate is a solid as opposed to brine or gas. By filling the pore space, gas hydrate acts to reduce the porosity available to the pore-fluid and, by so doing, increases the elastic moduli of the solid frame. It is difficult to reconcile this effect with more recent observations that the attenuation of elastic waves grows with increasing gas hydrate concentration.

Indeed, intuitively, one would expect that the stiffer the rock the smaller the relative elastic energy losses per cycle and, therefore, the smaller the attenuation. Measurements in many sediments support this intuition. For example, Klimentos and McCann (1990) show that attenuation increases with increasing porosity and clay content while the velocity behaves in an opposite way. Koesoemadinata and McMechan (2001) who statistically generalized many experimental data point to the same fact. This intuition, combined with quantitative modeling, led Dvorkin et al. (2003) to suggest reduced absorption as a possible seismic attribute for methane hydrate detection.

However, the facts are persistent. Unexpectedly large attenuation in sediments with gas hydrates has recently been observed at different geographical locations, in different depositional environments, and at different frequencies. In 1999, Guerin et al. presented qualitative evidence of dipole waveform attenuation in the hydrate-bearing sediments in the Outer Blake Ridge. Sakai (1999) noted that the shear-wave VSP signal may be strongly attenuated in a Mallik well within the methane-hydrate interval. Wood et al. (2000) observed increased attenuation of seismic waves at the same location. Guerin and Goldberg (2002) used monopole and dipole waveforms to quantify compressional- and shear-wave attenuation. They reported a monotonic increase in both with increasing hydrate saturation.

Pratt et al. (2003) reported an increase in attenuation in the Mallik hydrate reservoir between two methane hydrate wells during cross-hole experiments in the 150 to 500 Hz frequency range. Anomalous absorption has been observed in the Nankai Trough methane hydrate reservoir in the seismic frequency range (M.T. Taner, personal

communication). We have no reason to question the validity of these field data and, therefore, concern ourselves with the task of establishing a plausible quantitative physical explanation and, by so doing, determine in which situations increased attenuation can be expected in methane hydrate.

Seismic energy in porous rock with fluid dissipates due to wave-induced oscillatory cross-flow. The viscous-flow friction irreversibly transfers part of the energy into heat. This flow may be especially strong in partially-saturated rock where the viscous fluid phase (water) moves in and out of the gas-saturated pore space.

Such viscous-friction losses may also occur in wet rock where elastic heterogeneity is present. Deformation due to a stress wave is relatively strong in the softer portion of the rock and weak in the stiffer portion. The spatial heterogeneity in the deformation of the solid frame forces the fluid to flow between the softer and stiffer portions. Such cross-flow may occur at all spatial scales.

Microscopic "squirt-flow" is developed at the sub-millimeter pore scale because a single pore may include compliant crack-like and stiff equi-dimensional parts. Macroscopic "squirt-flow" which is more relevant to the seismic prospecting scale, may occur due to elastic heterogeneity in the rock frame. This mechanism has recently received a rigorous mathematical treatment by Pride et al. (2003) in a "double-porosity" model.

However, there is a simple way of quantifying the effect of macroscopic "squirt-flow" on seismic wave attenuation. Recall that in a viscoelastic body causality requires that there be a very specific relation between attenuation and frequency-related velocity (or elastic modulus) change. This relation is referred to as the Kramers-Kronig equation. It implies that a larger attenuation generally is associated with a larger wave-speed change between low frequency and high frequency. It has an especially simple expression in the standard linear solid:

$$Q_{Max}^{-1} = \frac{1}{2}\frac{M_H - M_L}{\sqrt{M_H M_L}}, \qquad \text{(AI-1)}$$

where Q_{Max}^{-1} is the maximum inverse quality factor (the ratio of the elastic energy dissipated per cycle of oscillation to the peak elastic energy during the cycle); M_H is the

compressional modulus at very high frequency; and M_L is the compressional modulus at very low frequency. M is the product of the bulk density and *P*-wave velocity squared.

Consider now a model rock that is fully water-saturated (wet) and has two parts. One part (80% of the rock volume) is shale with porosity 0.4; clay content 0.8 (the rest is quartz); and the *P*-wave velocity 1.9 km/s. The other part (the remaining 20%) is clean high-porosity slightly-cemented sand with porosity 0.3 and the *P*-wave velocity 3.4 km/s. The compressional modulus is 7 GPa in the shale and 25 GPa in the sand. Because of the difference between the compliance of the sand and shale parts, their deformation due to a passing wave is different, leading to macroscopic "squirt-flow."

At high frequency, there is essentially no cross-flow between sand and shale simply because the flow cannot fully develop during the short cycle of oscillation. The effective elastic modulus of the system is the harmonic (Backus) average of the moduli of the two parts: M_H = 16 GPa.

At low frequency, the cross-flow can easily develop. In this case, the fluid reacts to the combined deformation of the sand and shale. The dry-frame compressional modulus in the shale is 2 GPa while that in the sand is 20 GPa. The dry-frame modulus of the combined dry frame – 7 GPa – is the harmonic average of the two. The arithmetically averaged porosity of the model rock is 0.32. To estimate the effective compressional modulus of the combined dry frame with water we theoretically substitute water into this combined dry frame. The result is M_L = 13 GPa. The calculated maximum inverse quality factor computed from M_H and M_L according to Equation AI-1 is Q_{Max}^{-1} = 0.12 which translates into a noticeable attenuation coefficient of about 0.02 dB/m. The above-described ad-hoc averaging technique for attenuation estimate in wet rock can be applied to well log curves by means of a moving averaging window.

Our *S*-wave attenuation model rests on laboratory and field evidence that Q_s: (a) weakly depends on water saturation and (b) approximately equals Q_p at 100% water saturation. Our theory assumes that: (a) Q_s is related to the shear-modulus-versus-frequency dispersion by the same viscoelastic model as Q_p (e.g., the standard linear solid) and (b) the shear-modulus-versus-frequency dispersion is linked to the compressional-modulus-versus-frequency dispersion.

To model this link, we assume that the reduction in the compressional modulus of wet rock between high frequency and low frequency is due to the introduction of a hypothetical set of defects (e.g., cracks). Next, we assume that the same set of defects is responsible for the reduction in the shear modulus between high frequency and low frequency. Then, by using (e.g.) Hudson's (1990) theory for cracked solid, we link the shear modulus versus frequency dispersion to that of the compressional modulus with the proportionality coefficient being a function of the V_p/V_s ratio. As a result,

$$\frac{Q_s}{Q_p} = \frac{5}{4}\frac{(\gamma-2)^2}{(\gamma-1)}/(\frac{2\gamma}{3\gamma-2}+\frac{\gamma}{3\gamma-3}), \quad \gamma \equiv \frac{V_p^2}{V_s^2}. \tag{AI-2}$$

The Q_s/Q_p ratio is about 1 for $V_p/V_s = 1.9$ or Poisson's ratio 0.3 which is typical for rock with water. This theory mimics the observation that $Q_s \approx Q_p$ in wet rock.

We apply this attenuation modeling to well log data from the Mallik 2L-38 well. The interval under examination includes several sand bodies whose pore space is partly filled with methane hydrate (Figure 10 in main text). The rock-frame porosity in these sands exceeds 30% and the measured *P*-wave impedance is much larger than in the surrounding shale or sand without hydrate. This impedance contrast gives rise to strong elastic heterogeneity in the interval.

For the purpose of attenuation calculation, the sediment in the interval is considered wet because it does not contain free gas. Then the methane hydrate has to be treated as part of the sediment's frame. Of course, where the hydrate is present, the porosity of this modified frame is smaller than that of the original frame composed of quartz and clay and equals the product of the original porosity and one minus methane hydrate saturation. Also, the effective solid-phase modulus of the modified frame has to include the component due to methane hydrate as described in main text. The pore fluid in this modified frame is water.

Our inverse quality factor estimation (Figure AI-1) shows that high attenuation occurs precisely where methane hydrate is present, the impedance contrast is large, and elastic heterogeneity is strong. This estimate quantitatively explains the observations that the amplitude loss is high in sediments with methane hydrate. The inverse quality values are not that different from the recent in-situ estimates of Pratt et al. (2003) obtained from

cross-hole waveform inversion data in a 150 to 500 Hz frequency range (Q^{-1} between 0.15 and 0.20 in the sands with methane hydrate and very small, less than 0.05 in the rest of the section).

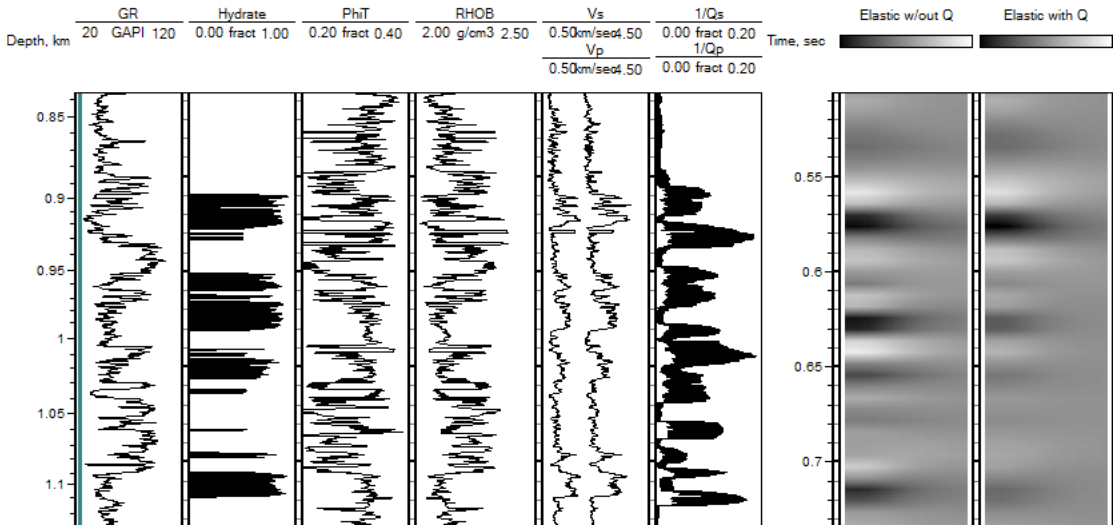

Figure AI-1. Well log curves in Mallik 2L-38 with calculated inverse quality factor shown in the sixth track (black for *P*-wave and white for *S*-wave). The migrated synthetic gathers with and without attenuation are shown on the right.

Full wave-form synthetic seismograms computed at the well with attenuation and without it show that attenuation indeed may affect the seismic amplitude in hydrate and thus has to be taken into account during quantitative reservoir characterization.

The self-induced elastic heterogeneity in a methane hydrate reservoir may also cause scattering attenuation. To estimate this contribution we use the O'Doherty-Anstey (1971) formula $Q^{-1} = 2\pi f \hat{I}(2f)$, where f is frequency and $\hat{I}$ is the power spectrum of the logarithmic impedance fluctuations of the medium $\ln(I_p) - \langle \ln(I_p) \rangle$. We estimate attenuation from scattering in the entire interval of Mallik 2L-38. Q^{-1} thus calculated appears as a single number for the entire interval because scattering attenuation is a layer property.

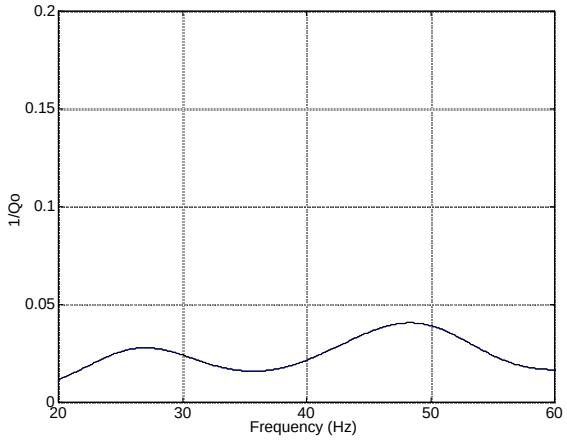

Figure AI-2. The inverse *P*-wave quality factor due to scattering in Mallik 2L-38.

The result (Figure AI-2), showing the scattering attenuation about a quarter of the macroscopic squirt flow attenuation, arguably has to be taken into account.

APPENDIX II. PROBLEMS OF SEISMIC RESOLUTION

Rock physics models are usually utilized on a point-by-point basis at the well log and/or core scale. The scale of seismic data may exceed these by two or three orders of magnitude. A seismic wave smears the small-scale elastic features. Sharp impedance contrasts associated with the presence of hydrate and free gas become smaller and may even disappear in impedance inversion volumes.

Consider a gas hydrate pseudo-well where the upper part of the sand body is filled with methane hydrate and the lower part contains free gas (Figure AII-1). The hydrate sand has large impedance and the free-gas sand has small Poisson's ratio.

The smoothing effect of the seismic wave on the elastic attributes (upscaling) simulated via Backus (1962) averaging of the elastic moduli by a running 5 m window is also displayed in Figure AII-1. The sharp impedance and Poisson's ratio contrasts apparent at the log scale become smaller. Even the vertical positions of the extrema of the upscaled elastic properties change. Figure AII-2 shows an I_p - ν cross-plot that can be used for identifying gas hydrate and free gas from acoustic and elastic impedance data. It is clear how the upscaling makes the clusters of data points that correspond to the hydrate and gas sand change their position in this diagnostics cross-plot.

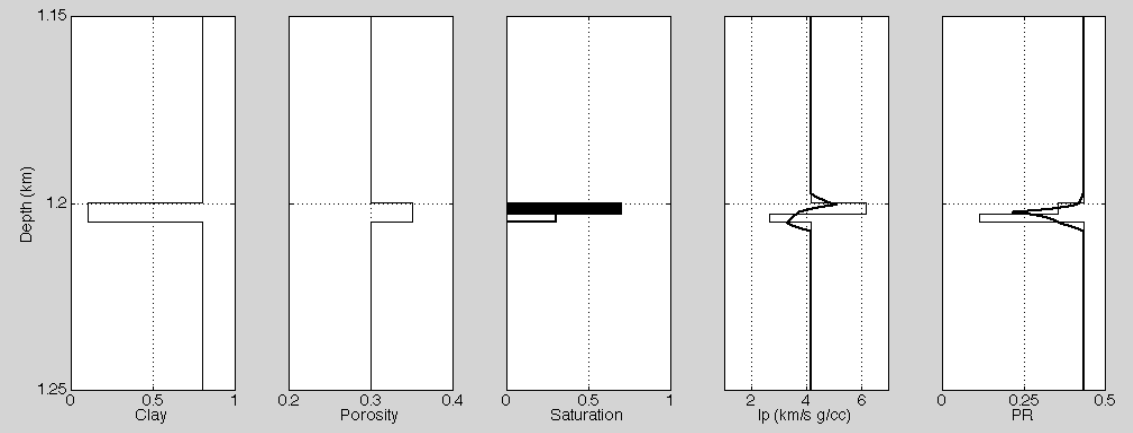

Figure AII-1. Pseudo-well with methane hydrate and free gas underneath. From left to right: clay content; total porosity; hydrate (black) and gas (white) saturation; P-wave impedance; and Poisson's ratio. In the last two frames the fine black curves are for the log data while the bold curves represent Backus-average upscaling.

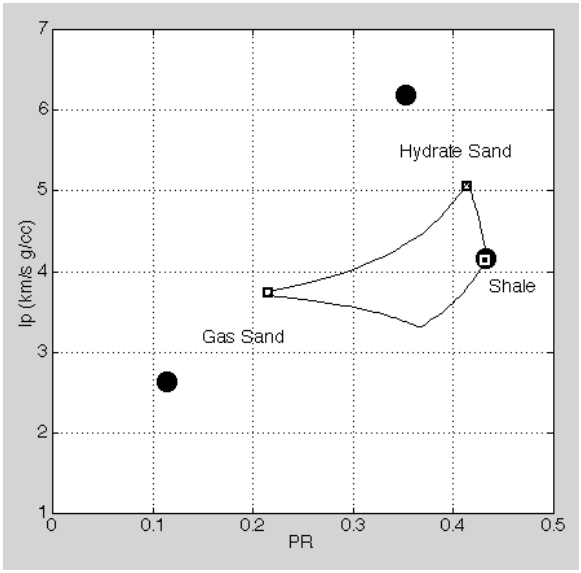

Figure AII-2. Impedance versus Poisson's ratio from pseudo-well data shown in Figure AII-1. Black symbols indicate the positions of the three lithofacies, shale, hydrate sand, and gas sand, at the log scale. Fine curves are the cross-plot of the upscaled elastic properties with open squares at the apexes. Transition from black symbols to open squares indicates the change in the positions of hydrate sand and gas sand due to this upscaling.

Because of the often complex stratigraphic distribution and thickness of sand/shale layers, there is no universal recipe for upscaling rock physics models and relations. The upscaling effect has to be evaluated in each concrete case by synthetic seismic modeling

or Backus averaging. The former could be especially revealing in assessing the effects of reservoir thickness.

Figure AII-3 displays the results of ray-tracer modeling on a pseudo-well with gradual reduction of the thickness of the hydrate and free gas layers. As a result of varying geometry, we observe dramatic changes in the seismic reflection.

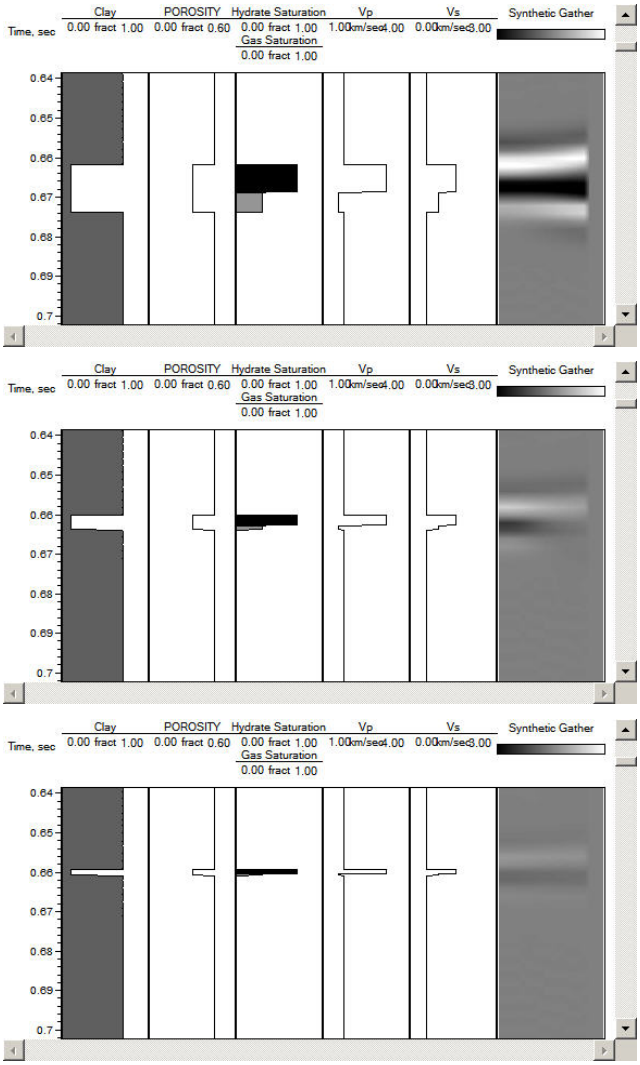

Figure AII-3. Synthetic seismic gather at a pseudo-well with thick (top) and thin (bottom) hydrate and free-gas sand layers.

APPENDIX III. MODEL FOR PURE HYDRATE DISPERSED IN SEDIMENT

One proposed mode of methane hydrate distribution in sediment is not within the pore space of the host frame but rather as macroscopic inclusions of pure hydrate in a

sediment background whose pore space does not contain methane hydrate. By assuming that this mixture is isotropic, we can immediately apply the Hashin-Shtrikman (1963) bounds to find the maximum and minimum possible bulk and shear modulus at a given hydrate concentration. The resulting equations for the effective bulk and shear moduli (K_{eff} and G_{eff}, respectively) are

$$
\begin{aligned}
&[\sum_{i=1}^{N}\frac{f_i}{K_i+\frac{4}{3}G_{\min}}]^{-1}-\frac{4}{3}G_{\min}\le K_{eff}\le[\sum_{i=1}^{N}\frac{f_i}{K_i+\frac{4}{3}G_{\max}}]^{-1}-\frac{4}{3}G_{\max},\\
&[\sum_{i=1}^{N}\frac{f_i}{G_i+Z_{\min}}]^{-1}-Z_{\min}\le G_{eff}\le[\sum_{i=1}^{N}\frac{f_i}{G_i+Z_{\max}}]^{-1}-Z_{\max},\\
&Z_{\max}=\frac{G_{\max}}{6}\left(\frac{9K_{\max}+8G_{\max}}{K_{\max}+2G_{\max}}\right),\quad Z_{\min}=\frac{G_{\min}}{6}\left(\frac{9K_{\min}+8G_{\min}}{K_{\min}+2G_{\min}}\right).
\end{aligned}
\qquad \text{(AIII-1)}
$$

where N is the number of the elastic components of a composite; f_i is the volumetric fraction of the i-th component; K_i and G_i are the bulk and shear moduli of the i-th component, respectively; and subscripts "max" and "min" refer to the maximum and minimum moduli, respectively.

Assume that the host sediment has porosity 0.4 and its mineralogy is 0.5 clay and 0. 5 quartz. Its bulk and shear moduli as calculated from the soft sand model are 5.57 and 0.84 GPa, respectively. Its bulk density is 1.98 g/cc and the velocity is 1.84 and 0.65 km/s for the P- and S-wave, respectively. The properties of methane hydrate are from Table 1. The resulting upper and lower bounds are plotted in Figure AIII-1 versus the hydrate concentration C_h in the whole rock. Because the elastic properties of the host sediment and pure hydrate in this example are close to each other, the upper and low bounds for the moduli and velocity of the sediment with hydrate are also close to each other, so that either one (or their arithmetic average) can be chosen as an estimate for the composite.

In the same figure, we plot the velocity according to the soft-sand (with hydrate) model. It strongly exceeds the velocity in sediment with dispersed hydrate for the same hydrate concentration.

Notice that hydrate concentration in the whole rock volume C_h is not the same as the hydrate saturation of the pore space S_h. The relation is $C_h=\phi_t S_h$, where ϕ_t is the total

porosity of the host sediment. This means that if the hydrate is located within the pore space of the host sediment, C_h cannot exceed ϕ_t simply because S_h cannot exceed one. However, if large fragments of pure hydrate are dispersed within host sediment, C_h can possibly reach one at the log measurement scale.

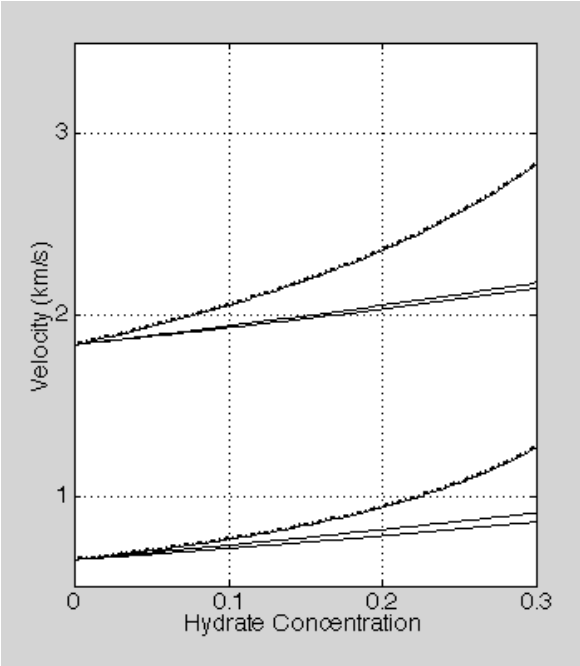

Figure AIII-1. Upper and lower Hashin-Shtrikman bounds for the P- and S-wave velocity (fine curves) as well as according to the soft-sand model (bold dash-dot curves) versus hydrate concentration in sediment.

National Energy Technology Laboratory

626 Cochrans Mill Road
P.O. Box 10940
Pittsburgh, PA 15236-0940

3610 Collins Ferry Road
P.O. Box 880
Morgantown, WV 26507-0880

One West Third Street, Suite 1400
Tulsa, OK 74103-3519

1450 Queen Avenue SW
Albany, OR 97321-2198

539 Duckering Bldg./UAF Campus
P.O. Box 750172
Fairbanks, AK 99775-0172

Visit the NETL website at:
www.netl.doe.gov

Customer Service:
1-800-553-7681